Studies of the Growth Conditions, Plasmonic and Magnetoplasmonic Properties of Semiconductor Nanostructures

by

Yunyan Wang

A thesis

presented to the University of Waterloo

in fulfillment of the

thesis requirement for the degree of

Master of Science

in

Chemistry

Waterloo, Ontario, Canada, 2018

Author's Declaration

I hereby declare that I am the sole author of this thesis. This is a true copy of the thesis, including any required final revisions, as accepted by my examiners.

I understand that my thesis may be made electronically available to the public.

Abstract

Magnetoplasmonic nanostructures, as a branch of multifunctional materials, have recently attracted research interests due to the coexistence of magnetic and plasmonic properties.[1-4] To accomplish the simultaneous control of both functionalities, appropriate design of the material construction is necessary. This study attempts to explore the magneto-optical properties of plasmonic semiconductor nanocrystals (NCs), specifically the behavior of the excitonic transition and its correlation with the magnetoplasmonic properties of NCs. Furthermore, considering the potential application for spintronic devices, one-dimensional nanowires (NWs) is one of the best platforms,as they have been widely exploited in optoelectronic and magnetoelectronic devices. Thus, the growth of plasmonic semiconductor nanowires is worthwhile to investigate.

The influence of localized surface plasmon resonance (LSPR) on magneto-optical properties are investigated in doped zinc oxide (ZnO) semiconductor NCs. ZnO, as a sort of n-type transparent conductive oxide (TCO), is an earth-abundant semiconductor with a direct band gap of 3.37 eV. In this study, indium-doped ZnO (IZO) and aluminum-doped ZnO (AZO) NCs have been successfully synthesized across various doping concentrations and all samples exhibit LSPR in the near-to-mid infrared region. For IZO NCs, the most intense plasmon absorption band is achieved for the sample with a starting In doping concentration at 10 %. A reduction of plasmon peak intensity occurs with a further increase of starting dopants concentration. However, for AZO NCs, the plasmon band continues to increase up to 30 % starting Al/Zn atomic ratio due to poor doping efficiency. The apparent blue shift of the band gap for both IZO and AZO NCs have been observed due to the Burstein-Moss effect. In the magnetic circular dichroism (MCD) spectra, the splitting of the excitonic transition under the external magnetic field indicates the complete

polarization of free carriers, which could be attributed to the phonon-mediated plasmon-exciton coupling. More importantly, the carrier polarization induced by plasmon-exciton coupling could be maintained at room temperature and low magnetic field (less than 1 T) showing great potential for its applications into new spintronic and optoelectronic devices.

In addition, the optimal growth conditions of gallium phosphide (GaP) NWs by the chemical vapor deposition (CVD) method are discussed as the initial step towards the synthesis of plasmonic III-V NWs. The growth of GaP NWs is generally accompanied by the unintentional formation of thick oxide coating, which may compromise the optical and electrical properties of NWs. Controlling and eliminating the as-formed outer layer during thermal evaporation growth of GaP NWs represents a barrier to the simple and scalable preparation of this technologically important material. The second part of this study systematically investigated the role of different parameters (temperature, hydrogen flow rate, and starting P/Ga ratio) in the synthesis of GaP nanowires, and mapped out the conditions for the growth of oxide-layer-free nanowires. Increasing all three parameters leads to diminished oxide layer thickness and improved nanowire morphology. Long and straight nanowires with near perfect stoichiometry and the complete absence of oxide outer layer are obtained for 1050 °C, 100 sccm hydrogen flow rate, and P/Ga flux ratio of 2.

Acknowledgements

I would like to express my particular gratitude to my supervisor, Dr. Pavle Radovanovic, for his patient guidance, enthusiastic encouragement, and immense knowledge. His continuous support throughout the whole project helped me overcome many challenges during my M.Sc. program.

My grateful thanks are also extended to my committee members, Dr. Jonathan Baugh, and Dr. Germán Sciaini, for their constructive comments, suggestions, and encouragement.

My sincere thanks also go to Dr. Carmen Andrei from McMaster University for her assistance in TEM image collection. I would like to acknowledge Kleinke's group and Nazar's group at the University of Waterloo, for their help on the XRD detection and FTIR measurement.

I would also like to extend my thanks to all my past and present group members, Manu, Terry, Vahid, Natalie, Paul, Hanbing, Susi, Enas, Yi, Shuoyuan, Johnathan, Nathaniel, and Luna. I highly appreciate their assistance and companion during my research. Especially Manu who gave me many insightful suggestions on the CVD programs. Also my sincere thanks to Terry's help on the MCD measurement and Hanbing's useful tips during data analysis.

Last but not least, heartfelt gratitude to my parents and my friends, who always support me and encourage me to achieve my goals despite the time difference and remote distance.

Table of Contents

List of Figures

List of Tables

List of Abbreviations

Acac	Acetylacetonate
AZO	Aluminum-doped Zinc Oxide
CVD	Chemical Vapor Deposition
EDX	Energy Dispersive X-ray Spectroscopy
Eq.	Equation
FTIR	Fourier Transform Infrared Spectroscopy
FWHM	Full Width at Half Maximum
HRTEM	High-Resolution Transmission Electron Microscopy
IZO	Indium-doped Zinc Oxide
LSPR	Localized Surface Plasmon Resonance
MBE	Molecular Beam Epitaxy
MCD	Magnetic Circular Dichroism
MIR	Mid-Infrared
NCs	Nanocrystals
NIR	Near-Infrared
NWs	Nanowires
PXRD	Powder X-ray Diffraction
SAED	Selected Area Electron Diffraction
SCCM	Standard Cubic Centimeters per Minute
SEM	Scanning Electron Microscopy
SPP	Surface Plasmon Polariton
SPR	Surface Plasmon Resonance
TCOs	Transparent Conductive Oxides
TEM	Transmission Electron Microscopy
UV-Vis-NIR	Ultraviolet-Visible- Near-Infrared Spectroscopy
VLS	Vapor-Liquid-Solid
WZ	Wurtzite
ZB	Zinc-Blende

Chapter 1 Introduction

1.1 Basic Introduction to Doped Semiconductor Nanomaterials

Nanostructured materials have a large surface to volume ratio and possibly exhibit the quantum confinement effect. These nanomaterials have drawn particular attention since they exhibit distinctly different properties from bulk materials such as surface and interface interactions, size-dependent physical properties, and quantum effect.[5] Because of these unique features, nanoparticles provide opportunities for various applications in practical devices. Nowadays, great research interest has been focused on semiconductor nanomaterials, for instance, nanocrystals (NCs) and nanowires (NWs), in applications such as biosensors, solar cells, and nanoelectronics.[6]

A semiconductor is a kind of material whose electrical conductivity is between an insulator and a conductor. Different semiconductor materials possess various conductivities, and they have a small band gap which is generated between the valence band, which is occupied with electrons, and the conduction band, which is empty.[7] The large band gap in an insulator makes it impossible to transfer electrons. Nevertheless, tiny band gap or even no band gap because of the overlap of the valence band and conduction band of a conductor guarantee it has very low resistance. In both cases, resistance is difficult to modify. However, with external biases or dopants, a change up to 10 orders of magnitude could occur for the conductivity of semiconductors.[6]

A natural semiconductor without doping is an intrinsic semiconductor whose charge carriers are resolved from their crystallographic structure; in contrast, a semiconductor whose properties result from the impurities doped into a host lattice is a kind of extrinsic semiconductor.[8] There are generally two types of doped semiconductors, classified as either n-type or p-type according to the

type of free carriers. An n-type semiconductor has its dopants providing extra electrons and their energy levels are close to the conduction band. However, in p-type semiconductors, there are fewer valence electrons in the dopants compared to the host materials. Dopant energy levels in p-type semiconductors are close to the valence band and give extra holes. Compared to bulk semiconductor materials, doped semiconductor nanoparticles possess unique properties. For instance, without thermal activation, dopants in nanoparticles can auto-ionize since the confinement energy overcomes the Coulomb interaction and hence takes up a confined electronic state automatically.[9]

Dopant ions in host semiconductor nanoparticles can go through either interstitial or substitutional doping, which occurs during the growth of host crystals or by partial ion exchange afterward. Typically, since dopants have different radii and valence states, strains will be introduced into the host materials which need further treatment to solve the mismatch. However, dopants may be removed due to the size mismatch, hence it is quite easy to accomplish doping for ions with a similar radius to the host nanoparticles.[10]

The doping mechanism of semiconductor nanomaterials has undergone several explanations. The Turnbull model suggested that doping of nanomaterials is dominated by statistics and there is no difference with bulk materials.[11] However, this model cannot describe the difference between bulk materials and nanoparticles in terms of different dopant solubilities. The self-purification model based on a thermodynamic growth implies that doping in nanoparticles is much more difficult than that into bulk materials due to high energy requirements along with expelled dopants to the surface of the nanoparticle.[10] Nevertheless, this model demands a thermodynamic equilibrium environment and the necessity of atomic exchanges which require a rapid diffusion of the dopant atoms through the host nanoparticle. Under this circumstance, an extraordinarily high

growth temperature is needed and this mechanism is more suitable for solid or gas phase synthesis. The mechanism of doped semiconductor nanoparticle growth in the liquid phase can be constructed through a kinetic control, named the trapped dopant model.[12] The activation barriers are key factors indicating that after adsorbing on the surface of the host nanoparticles, dopants will be further trapped. Doping efficiency, in this case, essentially depends on the shape of the nanoparticles, the crystal structure, and the existence of appropriate surfactants.

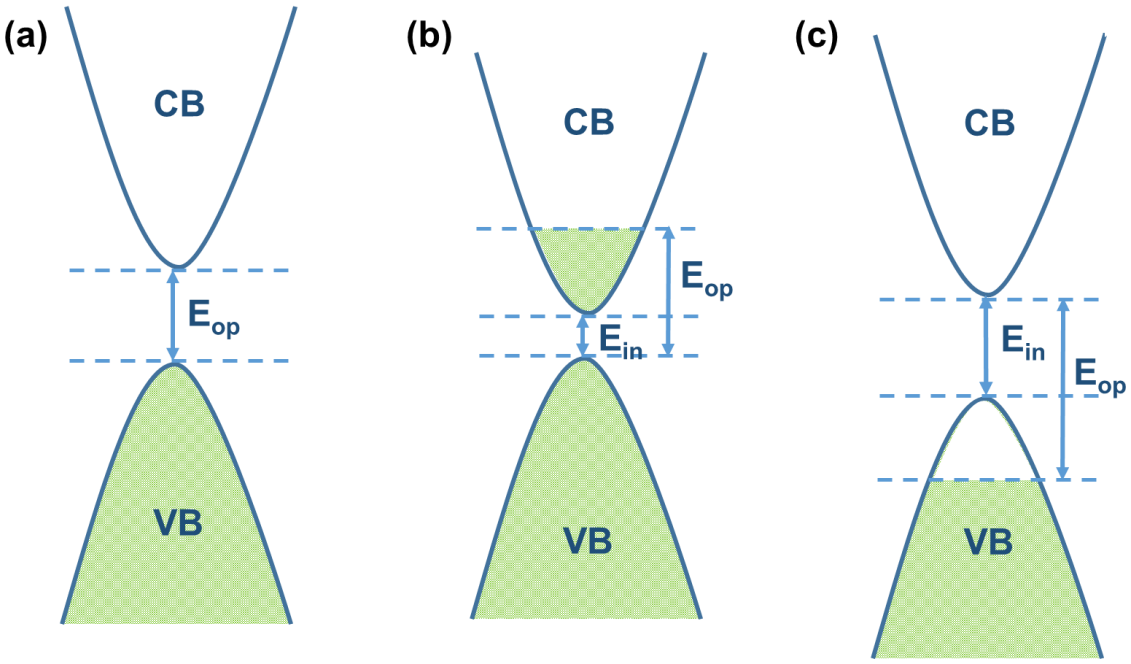

Figure 1.1 Illustrations of the band structure for (a) pure nanoparticles, (b) n-type semiconductor nanoparticles, the intrinsic band gap is smaller than undoped samples, because of the filling of the conduction band, the optical band gap increases. (c) p-type semiconductor nanoparticles, both the intrinsic band gap and the optical band gap will increase with the increasing holes.

When doping with aliovalent ions, a shift occurs in the apparent optical band gap of semiconductor nanomaterials, known as the Burstein-Moss effect.[13] This variation of the band gap

depends on free carrier concentration. Figure 1.1 illustrates the effect of different dopants on the intrinsic band gap and the optical band gap of semiconductor nanoparticles. For n-type semiconductor nanoparticles around degenerate doping, extra electrons from the dopants occupy the bottom of the conduction band, result in the change of the lattice parameters which slightly decrease the intrinsic band gap. However, the additional energy from the highest occupied state to the bottom of the conduction band accounts for the increase in the optical band gap, while for p-type semiconductor nanoparticles, both intrinsic and optical band gaps will increase due to the formation of holes in the valence band which decreases the highest occupied states. Other than the Burstein-Moss effect, the band gap of semiconductor nanomaterials can also be impacted by several factors such as quantum size confinement, band shallow acceptor transition, and impurity band formation.[14,15]

1.2 Localized Surface Plasmon Resonance (LSPR)

A plasmon is a quantum of plasma oscillation which can also be represented as a collective oscillation of the free electrons.[16] When the resonant oscillations of electrons stimulated by incident light proceed on the surface of a material or the interface between a dielectric and a conductor, it forms the surface plasmon resonance (SPR).[17] As the surface plasmon is restricted in a nanoparticle whose frequency is comparable with the wavelength of light, the free electrons inside the particle could take part in the oscillation which introduces the localized surface plasmon resonance (LSPR).[16] Propagating electromagnetic excitations in planar interfaces, such as extended metal films, forms the surface plasmon polariton (SPP).[18]

As illustrated in Figure 1.2, the plasmon oscillation stimulated by the oscillation of the incoming electromagnetic wave, which results in a displacement of the carriers and thus the

positive nuclei act as the restoring force and net charges exist around the surface of the nanoparticle. For LSPR, the electric field on the surface of the particle is highly enhanced, while a swift drop will occur with the increased distance from the surface. Plasmonic NCs have drawn immense research interests in recent years due to their wide range of possible applications in different fields. For example, the high optical sensitivity of plasmonic NCs to the surrounding environment makes them useful in chemical probes;[19] the ability to absorb in the infrared portion of the solar spectrum is suitable for solar cells;[20] and the reasonable penetration depth of the infrared light makes plasmonics possible to be applied in biological tissues.[21]

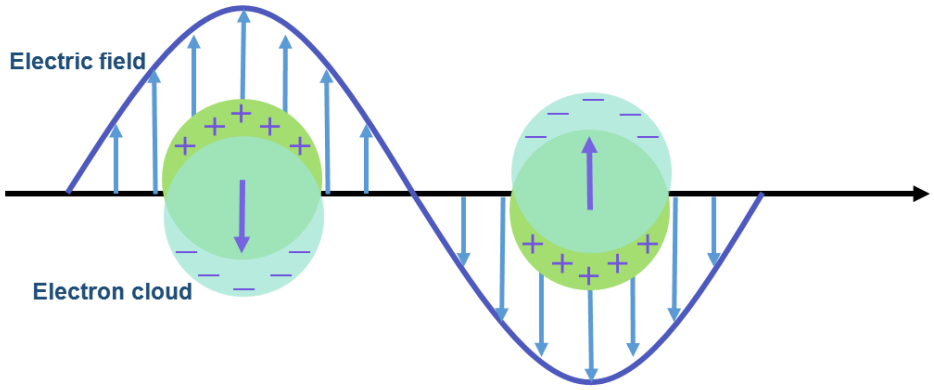

Figure 1.2 Plasmon oscillation of a spherical nanoparticle. The oscillations of electrons are initiated by the incoming electromagnetic wave.

LSPR was first discovered in traditional noble metal nanostructures such as silver and gold NCs. They have large carrier densities of about 10^{23} cm^{-3} and exhibit LSPR mostly in the visible and near-infrared regions. Their LSPRs are naturally in the static state based on their intrinsic size, shape, and composition.[22] After synthesis, the LSPR spectrum cannot be further modified. Several drawbacks exist in these materials,for example, there are high optical losses among electronic transitions, and they have an excessively high cost preventing them from the application into most

optical devices. Therefore, new types of materials which are capable of exhibiting the LSPR are essential to apply to different fields.

The discovery of LSPR in copper sulfide ($Cu_{2-x}S$)[23] makes copper deficient copper chalcogenides promising self-doped materials. They are considered as p-type doped semiconductor NCs with holes created in the valence band by removing copper atoms. Another type of popular materials is doped transparent conductive oxides (TCOs) since they possess high electrical conductivity and high transmission in the visible spectrum. The charge carrier of doped TCOs can be varied from 10^{16} to 10^{21} cm^{-3}, and the LSPR mainly locates in the near-infrared (NIR) and middle-infrared (MIR) region.[22] Doped TCOs have been extensively studied in a large amount of materials such as indium doped tin oxide (ITO), aluminum doped zinc oxide (AZO), antimony doped tin oxide (ATO), and antimony doped indium oxide (AIO).[24-26] The LSPR of these materials can be modified by electrochemical means or further redox doping processes, making it possible to realize the on/off switch of LSPR and hence motivates a wide range of practical applications.[22]

The LSPR properties in semiconductor NCs can be adjusted based on the variation of the particle shape, size, dopants segregation, and defect concentration.[27] Of these effects, the main factor directly influencing the LSPR frequency is the free carrier concentration. According to the Drude- Lorentz theory, the absorption coefficient (α) for LSPR has a direct linear relationship with the charge carrier concentration (n), as illustrated in equation 1.1[28]:

$$\alpha_{free-electrons} = \frac{ne^2}{m^*\varepsilon_0 Nc\tau\omega^2} \qquad \textbf{eq. 1.1}$$

where e is the unit of elementary charge, m^* is the effective mass of charge carriers, ε_0 is the permittivity of free space, N is the refractive index of the undoped semiconductor, τ is the mean time between two electron scattering events, and c and ω are the speed and frequency of light,

respectively. Meanwhile, in bulk materials, the plasma frequency ω_p, which describes the resonance frequency of free carriers, is shown in equation 1.2 [29]:

$$\omega_p = \sqrt{\frac{ne^2}{\varepsilon_0 m^*}} \qquad \textbf{eq. 1.2}$$

This equation clearly reveals that the concentration of charge carriers is straightforwardly related to the plasma frequency. In semiconductor NCs, the localized resonance ω_{sp}, which is modified from the bulk frequency, can be described as the following equation[29]:

$$\omega_{sp} = \sqrt{\frac{{\omega_p}^2}{1+2\varepsilon_m} - {\gamma_b}^2} \qquad \textbf{eq. 1.3}$$

where ε_m is the dielectric constant of the surrounding medium and γ_b is the bulk scattering frequency related to carrier dampening. These equations are derived from a simplified Drude model which ignores the geometrical considerations and are most suitable for spherical particles. It should be noticed that equation 1.3 demonstrates the impact of surrounding medium on the LSPR. When increasing the surrounding medium dielectric constant ε_m, the coulombic restoring force on the electron cloud will decrease, hence decrease the intensity of localized resonance.[30] The high sensitivity of the plasmon resonance to the surrounding medium ε_m is due to the near-field effect.[31] The near-field effect is activated by the displacement of the charges in NCs, which generates an oscillating field upon the LSPR and extends into the surrounding NCs. The external electric field will improve the near-field effect to orders of magnitude. However, this effect drops off exponentially when far away from the surface of the NCs. The damping factor γ related to γ_b in equation 1.3 is a sum of broadening factors that influence the collective oscillations of the carriers, which can be written as equation 1.4:

$$\gamma = \gamma_{e-e} + \gamma_{e-phonon} + \gamma_{e-defect} + \gamma_{e-surface} \qquad \textbf{eq. 1.4}$$

The equation shows that the carrier damping is introduced by the scattering of electrons, phonons, lattice defects, and surface impurities.[32] The damping factor, γ is related to the quality factor of an LSPR and affects the width of the plasmon resonance. The quality factor is the ratio of the plasmon peak energy to the full width at half maximum (FWHM) of the resonance peak. A higher quality factor implies a stronger plasmonic resonance, while a higher damping factor suggests a broader LSPR peak. With a high doping concentration, the size of NCs will be surpassed by effective path length of the electrons and the surface scattering can not be neglected which increase the damping factor γ. In this circumstance, according to equation 1.3, the LSPR frequency will decrease. This influence explains that in most cases, the doping concentration of semiconductor NCs can only be achieved at a low degree.

1.3 Multifunctional Nanomaterials and Zinc Oxide Nanocrystals

Aside from plasmonic properties, more attention has been concentrated on the integration of different functionalities into a single nanostructure system. Among these multifunctional materials, magneto-plasmonics have drawn particular attention because of the unique property of controlling optical properties with external magnetic fields.[33] The main focuses in the field of magneto-plasmonics include the effect of the magnetic fields on the SPR, the enhancement of the magneto-optical effects in plasmonic nanostructures, and also the generation of spintronic materials with the help of plasmons.[1,2,34] Based on these properties, applications such as light transmission and reflection modulators and biochemical sensors can be realized.

As illustrated in Figure 1.3, the first observation of optical properties modified by the magnetic field is the Faraday effect and the surface magneto-optical Kerr effect.[35] When the linearly polarized incident light comes to the magnetic medium, the polarization state of the

transmitted (Faraday) or reflected (Kerr) light will rotate due to the different propagation speeds of left and right circularly polarized lights. Faraday-effect occurs when the magnetic field is applied in the propagation direction, while the Kerr effect may appear as polar, longitudinal, or transversal configuration when the magnetic field is perpendicular to the reflection surface and parallel to the incident plane, parallel to both reflection surface and incident plane, or parallel to the reflection surface and perpendicular to the incident plane, respectively. Typically, the polar Kerr effect results in a large rotation of the polarization of the reflected light and only a slight rotation occurs in the transversal Kerr effect.[33]

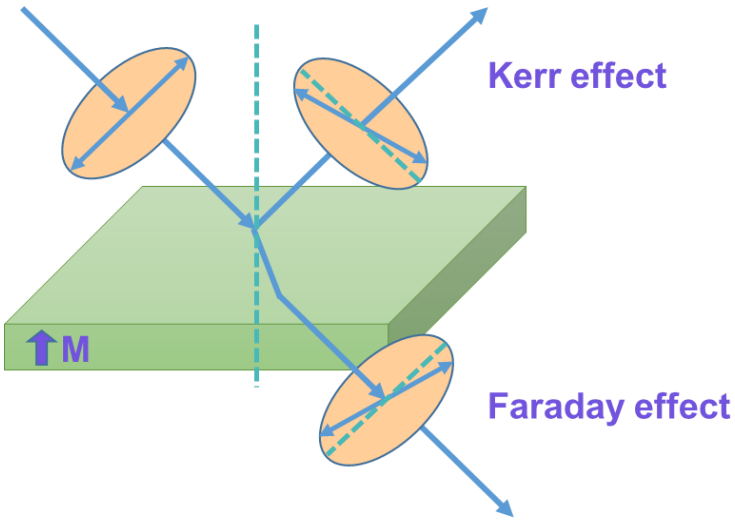

Figure 1.3 Schematic of the Faraday effect and the Kerr effect. For Faraday effect, the polarization of the transmitted light will rotate with an angle θ_F, and for Kerr effect, the polarization of the reflected light will rotate with an angle θ_K.

The earlier study on modification of the plasmonic properties in the magnetic field was focused on heavily doped semiconductors with surface plasmons in the far infrared region.[36] The

localization and propagation of surface plasmons can be adjusted by the external magnetic field because of the orientation between magnetic field and surface plasmon wave factor. On the other hand, plasmonic properties can affect the magneto-optical nanostructure by the induced phase modification of transmitted or reflected light, and this can be applied to the memory storage technology in which the plasmonic resonances play an important role by means of reducing the device size.[3,4] In addition, because of the strong near-field dipole-dipole magnetic coupling between closely spaced nanoparticles, the spintronic-plasmonic interactions are realizable in subwavelength size metallic materials with high electromagnetic transparency. Since the electromagnetic propagation can be modified in the dipole field of induced surface charges, the electrical, magnetic, and optical properties of the magneto-plasmonic materials are highly sensitive to each other. [37]

To achieve the modification of plasmonic properties, a large magnetic field is needed, as well as a small optical loss. Hence, the heterostructure of ferromagnetic materials and noble metals are often applied to this field, either via a core-shell or a heterojunction configuration.[38,39] However, there still lacks the study of the LSPR properties of doped TCOs under an external magnetic field. Meanwhile, the free coupling between LSPR and excitons, which has been used to enhance the excitonic absorption and emission, has attracted many research interests.[34,40] With the help of magnetic circular dichroism (MCD) spectroscopy, the magnetoplasmonic properties can be measured on simple colloidal noble metal NCs, where the LSPR of these NCs can be modified under an external magnetic field of 1 T. [41] The detection can be achieved because when the LSPR is optically excited, the movement of conduction electrons in the magnetic field gives rise to an increase in the magnetic force.[40,41] The capability to detect electron polarization in NCs due to

LSPR in MCD spectroscopy makes it possible to study the relationship between the plasmon and exciton.

MCD spectroscopy shows the different absorption of left (ρ^-) and right (ρ^+) circularly polarized light as the degree of ellipticity with the external magnetic field parallel to the light propagation direction. Magnetism of both solution and solid-state samples can be detected using the MCD spectroscopy. High resolution and fine structure can be obtained by the MCD spectra, as well as the detailed electronic structure. It is multidimensional and could study the ground and excited state Zeeman splitting simultaneously.The intensity of MCD (ΔA) can be described as:

$$\frac{\Delta A}{E} = \gamma \mu_B B[A_1\left(-\frac{\partial f(E)}{\partial E}\right) + \left(B_0 + \frac{C_0}{kT}\right) f(E)] \qquad \textbf{eq. 1.5}$$

Where E= *h*v, γ is coefficient factor, μ_B is the Bohr magneton, B is the applied magnetic field. A_1, B_0, and C_0 are the MCD A-, B-, C- term, respectively, *f*(E) is the absorption spectrum band shape, and $\frac{\partial f(E)}{\partial E}$ is the first derivative of *f*(E). The molecule should have degenerated excited states because of the Zeeman effect in A-term MCD, and due to the small amount of Zeeman splitting which in the range of several wavenumbers, opposite sign of the left and right circularly polarized result in a derivative band shape. According to equation 1.5, when change the temperature, there are no effect on the A-term MCD, hence it is temperature independent. In the B-term MCD, an intermediate state existing either close to the ground or the exited state lead to an absorption band shape. While in the C-term MCD, Zeeman splitting result in a degenerate ground state and this term only exhibited by paramagnetic materials. Again an absorption band shape exists in the C-term MCD since under low temperature, *kT* is comparable to the magnitude of Zeeman splitting in a strong magnetic field.[42]

For nanoparticles that have plasmonic properties, when an external electric field and a magnetic field are applied, the Lorentz forces on free carriers can be expressed as[43]:

$$F = F_E + F_B = q\mathbf{E} + q(v \times \mathbf{B}) \qquad \textbf{eq. 1.6}$$

where q is the charge of a carrier, **E** and **B** are electric and magnetic fields, respectively. The circularly polarized light induces the electric forces F_E. When the carriers have a velocity in the magnetic field, the magnetic forces F_B can be generated. These two forces are either in the same or opposite direction for left and right circularly polarized light which result in different frequencies, which can be written as[43]:

$$\omega = \omega_0 \mp \frac{q\boldsymbol{B}}{2m^*} \qquad \textbf{eq. 1.7}$$

The MCD signal shows the difference between the two absorptions, hence the intensity should be proportional to $\frac{q\boldsymbol{B}}{m^*}$, indicating a linear relationship between the plasmonic properties and external magnetic field in MCD spectra.

ZnO is an n-type II-VI semiconductor crystallizing in a wurtzite hexagonal structure. Compared to other TCO materials, ZnO is widely studied because it is an earth abundant material which has low cost and less toxicity, as well as physical and chemical stability. In addition, ZnO is a promising material due to the direct wide band gap of 3.37 eV at room temperature, high refractive index of 1.99, and large exciton binding energy around 60 meV.[43] The application of ZnO includes optoelectronic devices, transistors, luminescence materials, and sensors.[44-46] When doped with aliovalent group III element (Al, Ga, and In) cations, ZnO based materials will have an increased charge carrier density and exhibit good LSPR behavior. In particular, the indium-doped ZnO (IZO) and aluminum-doped ZnO (AZO) are very attractive materials since they have shown commendable LSPR properties. [24,47-49]

Several colloidal synthetic methodologies have been developed to obtain doped TCO nanoparticles. A sol-gel method can be applied to synthesize the metal oxide that uses the colloidal suspension (sol) with monomers as the precursor and then transfers into an integrated network (gel). Hot-injection synthesis allows dropwise injection of the dopant precursors into the hot reaction mixture during the synthesis period. Nevertheless, because of the inherent non-scalability, this method is not sufficient in the industry. A heat-up or non-injection method can also be applied for the preparation of doped ZnO NCs which mixes all the reactants together before heating. With careful control of the reaction kinetics, this method enables a large doping concentration with low reaction temperature and has been adopted in this study.[50]

1.4 Gallium Phosphide and III-V Semiconductor Nanowires

Besides nanoparticles, one-dimensional (1D) semiconductor nanostructures are also promising multifunctional materials. Beginning from carbon nanotubes, 1D semiconductor nanostructures have attracted intense research focus due to their unique properties on manufacturing nanoscale electronics and mesoscopic devices. 1D nanostructures are crucial to the integration and function of devices since they are anticipated to be the smallest dimension structures for optical excitations and efficient transport of electrons.

Among 1D nanostructures, such as tubes, rods, wires, and belts, semiconductor nanowires (NWs) have been extensively studied since they possess mechanical flexibility, which could be used for flexible electronics; and high surface-to-volume ratios, which could be applied to high-performance sensors.[1] The diameter of NWs is in the order of nanometers while the length of NWs often in the range of micrometers. Besides simple structures, NWs can also exist in the construction of heterojunctions, coaxial, hollow, and p-n junctions.[51] Compared to thin films, NWs can usually

be synthesized with a faster growth rate at lower growth temperatures. Moreover, NWs can grow on arbitrary substrates and can sustain more strain than thin films. Normally, crystallization is the key step of 1D nanostructure growth and the growth of NWs should be thermodynamically favorable to achieve the lowest Gibbs free energy possible.[52]

III-V semiconductor NWs have drawn research interests for their capability of lattice engineering and flexibility of band gap modification.[51] Among various 1D materials synthesized and investigated over the past two decades, III-V semiconductor NWs have shown particular versatility for applications in optoelectronics, including solar cells, light emitting diodes, lasers, photodetectors, and spintronic devices.[53-56] III-V bulk materials often exhibit a cubic zinc blende (ZB) crystal structure since the ZB structure is thermodynamically stable. Nevertheless, III-V NWs are capable of possessing both ZB structure and hexagonal wurtzite (WZ) structure as illustrated in Figure 1.4. Moreover, it is possible to alternate the crystal structures of III-V NWs by controlling the growth conditions, such as III/V ratio, growth temperature and doping concentration.[57]

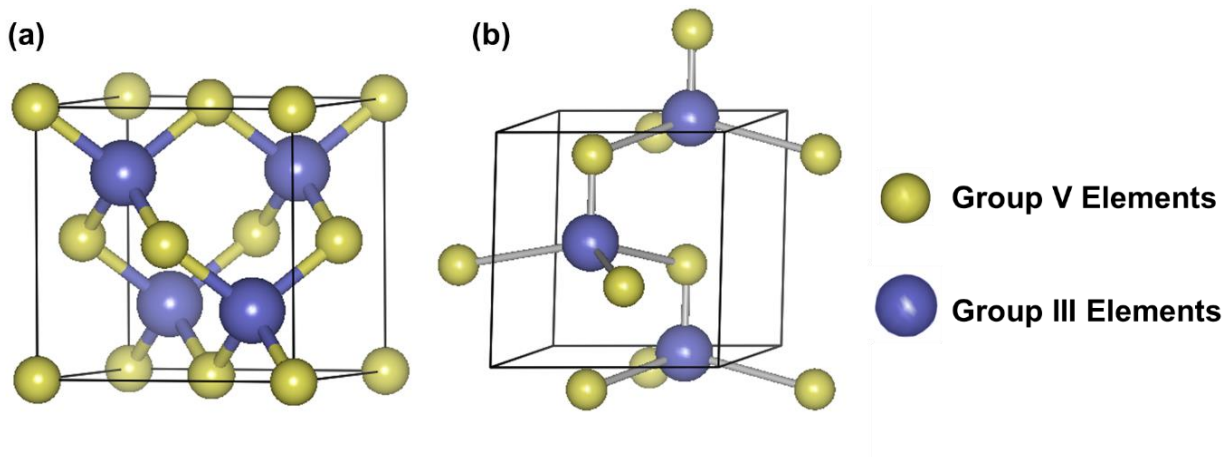

Figure 1.4 Illustration of (a) zinc blende crystal structure and (b) wurtzite crystal structure, where the large blue spots represent group III elements and small yellow spots group V elements.

ZB and WZ structures have different stack sequence along the growth direction. Typically, ZB structure stacks as ABCABC … and WZ structure stacks as ABAB…. Faulty stacking can happen during the growth process. Twin planes occur in the ZB structure as ABACACA…, and the C plane can be tilted by some degree. While misplacing a single layer may appear in the WZ structure as ABACAC…, which construct a ZB segment.[51] When growing NWs, the total free energy largely depends on the energy of solid and liquid interface, making it possible to grow along one direction. For ZB structure, the <111> direction has the minimum interface energy, and for WZ structure, the <001> direction commonly appears.[58,59]

As one of the III-V semiconductors, the interest in GaP NWs stems from its relatively indirect band gap (2.26 eV) in the ZB structure.[60] GaP NWs have the possibility of emitting different colors and the ability to introduce both electrons and holes as majority charge carriers.[61-63] These properties make GaP NWs promising materials for the prospective applications in optoelectronic and nanoelectronic devices. Additionally, GaP-based ternary and quaternary semiconductors are promising materials for multi-junction solar cell applications.[64] In the field of photovoltaic, GaP NWs have low-temperature deposition and are relatively low price; moreover, they are capable of growing on different substrates, which makes them valuable in various commercial applications.[65]

1.5 Growth Mechanism of Nanowires

Nanostructure semiconductors can be approached through top-down or bottom-up method.[66] Traditionally, the top-up method through lithographic techniques for bulk materials, the desired nanostructure could be obtained. Nevertheless, with a decrease in the length scale, the quality and

the uniformity of the structures are difficult to manipulate. On the contrary, the low-cost bottom-up method mostly relies on the self-assembling of atoms and it can reach small size scale precisely. Several strategies have been proposed under this approach. For instance, the 1D structure can be obtained by the self-assembly from 0D nanomaterials; seed symmetry of 1D growth can be adjusted by the liquid-solid interface; multiple templates can guide the 1D morphologies, and intrinsically anisotropic crystallographic structure can be used during the growth.[67] Among these mechanisms, the majority of gas phase preparations involve the vapor-liquid-solid (VLS) process, enabled by a pre-deposited metal nanocluster catalyst or self-assisted growth.

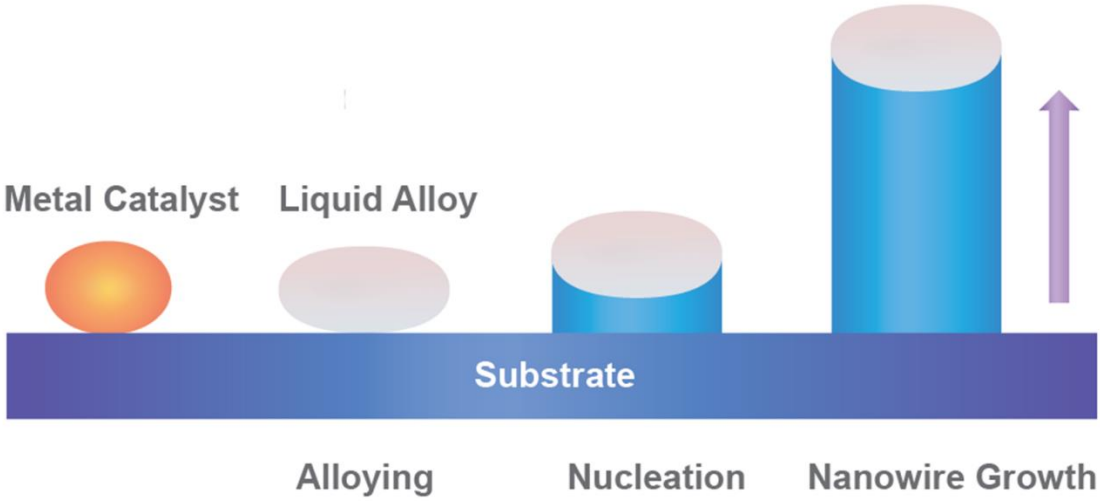

Figure 1.5 Illustration of the growth of nanowires via VLS mechanism. A liquid alloy will form after heating the metal catalyst above the eutectic temperature. When the liquid alloy supersaturates, the NWs will grow in the axial direction after nucleation.

First proposed in the 1960s by Wagner et al, the VLS mechanism was applied to explain the growth in silicon whiskers.[68] Since then, the VLS mechanism has been extended into 1D NW growth. The basic idea for the metal catalyst assisted VLS process is to add gaseous reactants into

a liquid phase metal catalyst to form a liquid alloy at the growth temperature. Taking the liquid alloy as a template, through nucleation at the solid-liquid interface, NWs will be developed by adsorption of the reactant vapor and its axial growth can be confined.[69] (Figure 1.5) Since the lowest energy barriers for nucleation occur at the three-phase boundary, the crystal will grow along one direction to form NWs rather than a 2D growth which leads to a planar structure.[70] Generally, the length of the NWs is managed by the growth time. During the growing process, NWs can grow with an unchanged diameter since it is mainly controlled by the size of the liquid alloy. However, some of the NWs also have radial growth, which forms a tapered structure for the whole wire.

Several experimental results indicate that the catalyst particle size can affect the axial growth rate of NWs.[71-73] The growth rate may increase or decrease with the increase of catalyst diameter, depending on the driving force during NW growth. Normally, the thermodynamic driving force of NW growth is the supersaturation, which is the chemical potential difference between the catalyst crystal phase and the reactant vapor pressure (equation 1.8):

$$\Delta\mu_{vc} = \mu_v - \mu_c \qquad \textbf{eq. 1.8}$$

Supersaturation can also be obtained by equation 1.9[73]**:**

$$\Delta\mu_{vc} = k_B T ln(\frac{p}{p_0}) \qquad \textbf{eq. 1.9}$$

Where *p* is the vapor phase adatom pressure and p_0 is the equilibrium vapor pressure in the catalyst particle. As the temperature increases, *p* will increase. NWs can be extended when $\Delta\mu_{vc}$ is positive and when $\Delta\mu_{vc}$ goes down to zero, the whole system will maintain in equilibrium and the growth of NWs will stop.

Choosing a suitable metal as the catalyst to cooperate with the reactants is an important step in this process since the catalyst should be inert to the chemical reaction, the solubility of the catalyst in the liquid phase should be high enough, and it also needs a low vapor pressure. The appropriate metal catalyst could be selected according to the equilibrium phase diagram.[70] Shown in Figure 1.6, in a pseudobinary phase diagram, when the catalyst and the reactants reach the eutectic point, NWs will growth. Hence it is important to choose a suitable catalyst whose melting point is within a reasonable range of temperature to enable the growth of NWs. Normally, transition metals or noble metals are qualified for III-V materials.

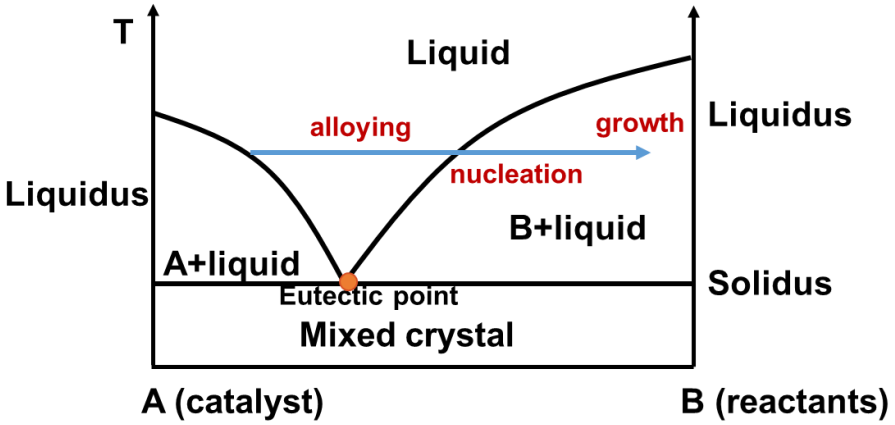

Figure 1.6 Schematic of a pseudobinary phase diagram. The orange spot represents the eutectic point where three phases coexist.

In addition to the growth of pure NWs, the incorporation of dopants into NWs has been generally applied in order to enhance optical and electrical properties and introduce magnetic properties. Doping can be achieved in NWs with high carrier concentration. Generally, dopants are imported from the gas phase and are incorporated into the NWs either through the liquid alloy from the axis growth or directly into the NWs from the radial growth. Some experimental studies have concluded that dopants are likely to bind on the surface of the NWs rather than going into the

core of NWs. This phenomenon is energetically favored and mostly suitable for NWs with short length.[52] A few results suggest that doping through radial growth is more efficient than that through axial growth. However, the axial growth may be restrained by the overgrowth in the radial direction which is undesired for some devices. Under this circumstance, *in situ* etching is introduced to prevent radial growth.[74]

In the radial direction, since dopants have different solid diffusivity, some of them are likely to enter NWs through diffusion from the side facets; while others may escape from the NWs through diffusion when there is not enough dopant precursor. Similarly, in the axial direction, there are two sorts of dopants. The first type of dopant possesses large solid segregation coefficient. Almost all the dopants can be transferred into the NWs with little re-evaporation. P-doped Si or Ge NWs belong to this kind of doping process. However, the second type of dopant has small solid segregation coefficients and high solubility in the liquid alloy. Re-evaporation cannot be ignored and only partial dopants enter the NWs through the liquid alloy. Sb-doped Ge NWs and Si-doped GaAs are representative examples of this doping process.[52]

Based on the VLS mechanism, the growth of NWs can be accomplished by molecular beam epitaxy (MBE), laser ablation, metalorganic chemical vapor deposition (MOCVD), chemical vapor deposition, etc.; [75-77] among these methods, CVD is particularly promising for commercially relevant applications because of the relatively low cost of the starting material, simplicity, safety, and the ability to grow NWs with different morphology on various substrates.[78,79] However, when growing GaP NWs, it will generally lead to the formation of thick oxygen-rich overlayers on the NW surface, which can be amorphous or crystalline and often consist of Ga_2O_3 and/or $GaPO_4$.[77,80-82] While this unintentionally formed shell could potentially be used as insulating oxide layers for

NW electronic devices, such as field effect transistors, the absorbed or incorporated oxygen could also compromise the inherent electrical and optical properties of GaP NWs. The rational and consistent control of the formation of this coating layer during NW growth has not yet been achieved.

1.6 Motivations and Scope of the Thesis

This study aims to explore the possibility of single-phase multifunctional nanostructures, to be specific, the plasmon-induced carrier polarization in plasmonic semiconductor nanomaterials. Magnetoplasmonic nanomaterials are promising materials which can be used in biochemical sensors, modulators, and quantum information processing devices.[1-3] Nevertheless, few studies have been focused on the magnetoplasmonic single-phase semiconductor nanomaterials due to the difficulty of establishing compatible experiments to demonstrate the interaction between the excitonic transition and magnetoplasmonic properties. This study attempts to investigate the relationship of these properties of semiconductor NCs and NWs.

The first part of this work concentrates on the plasmonic and magnetoplasmonic properties of indium-doped and aluminum doped ZnO NCs. ZnO is a kind of n-type TCO which is an earth-abundant semiconductor with a direct wide band gap of 3.37 eV. Using group III elements as the doping cations, ZnO based colloidal NCs are capable of generating intense tunable LSPRs. With the help of MCD spectroscopy, it is possible to discover the magnetoplasmonic-exciton coupling for doped ZnO NCs.

In addition, 1D NWs are promising materials for multifunctional studies as they have been widely exploited in optoelectronic and magnetoelectronic devices. For III-V semiconductor NWs, there are various applications in optoelectronics, including solar cells, spintronic devices, and

photodetectors.[55,83,84] The plasmonic properties have been successfully accomplished in doped GaN[85], indicating the immense research value on III-V NWs. The second part of this study is associated with the control of the spontaneous formation of oxide overlayers on GaP NWs grown by CVD. Without oxide shells, GaP NWs can then be further applied to various applications.

To study the crystal structures, morphologies, and optical properties in these nanoparticles, multiple characterization methods are applied. Based on the performed analysis, the plasmonic and magneto-plasmonic properties of doped ZnO NCs are discussed. The capability of controlling the behavior of the excitonic transition with the magnetoplasmonic properties makes these NCs promising materials in practical applications. Meanwhile, the inexpensive route of controlled growth of GaP NWs without oxide layers using the CVD method suggests effective improvement of the NW growth conditions.

Chapter 2 Experimental Method

2.1 Materials

All the chemical reagents and solvents were used as received from the manufacturers without any future purification. Gallium phosphide (GaP, 99.99% trace metal basis) and phosphorous (P, 97%) were purchased from Sigma-Aldrich. Gallium metal (Ga, 99.99%), aluminum acetylacetonate ($Al(acac)_3$, $Al(CH_3COCH=COCH_3)_3$, 99%), and indium acetylacetonate ($In(acac)_3$, $In(CH_3COCH=COCH_3)_3$, 98%) were obtained from Strem Chemicals. Zinc stearate ($Zn[CH_3(CH_2)_{16}COO]_2$, $ZnSt_2$, 12.5-14%) was purchased from Alfa Aesar. Oleic acid (OA, $CH_3(CH_2)_7CH=CH(CH_2)_7COOH$, 90%), 1-octadecene (ODE, $CH_3(CH_2)_{15}CH=CH_2$, 90%), 1-dodecanol (DDOL, $CH_3(CH_2)_{11}OH$, 98%), toluene (99.9%), hexane (98.5%) and acetone (99.9%) were also obtained from Sigma-Aldrich used as the solvents. Hydrogen (H_2) and argon (Ar) as the high purity carrier gases (grade 5), were obtained from Praxair.

2.2 Synthesis Methods

2.2.1 Synthesis of Doped Zinc Oxide Nanocrystals

The synthesis of doped zinc oxide NCs was mainly based on a non-injection method.[50] Typically, 1.89g $ZnSt_2$ and a desired amount of dopant ($In(acac)_3$ or $Al(acac)_3$) were added to a three neck round bottom flask to make a series of IZO or AZO up to 30 % doping concentration. Thereafter 2.65 g OA, 16 g ODE, and 4.8 g DDOL were added to the flask successively. Under room temperature with a reasonably stirring, the flask was degassed for 5 minutes and purged with argon gas for 10 minutes. After repeating the degassing and purging process twice, the flask was

kept under the argon atmosphere during the whole reaction. The solution was firstly increased to 140 ^{o}C and remained for 30 minutes to make sure all the precursors mixed and dissolved evenly. Henceforth, the temperature of the solution increased to 250 ^{o}C at 4 ^{o}C per minute. The reaction remained for 3 hours at 250 ^{o}C and then cooled down to room temperature. The precipitate was obtained by centrifuge and continuously washed with toluene and acetone three times. Finally, two equal parts of the precipitate were dispersed in toluene and hexane separately and the remainder was dried with acetone and then crushed for future measurement.

The synthesis reaction is an alcoholysis dominate reaction. According to the hard-soft acid-base theory, the group III dopants (Al^{3+}, In^{3+}) are harder than Zn^{2+}, which makes it easier for $ZnSt_2$ to interact with group III acetylacetonates. The typical reaction mechanism can be described as equation 2.1, 2.2 and 2.3:

$$\mathrm{Zn(OOC}-R_1)_2 + 2\,R_2-OH \rightarrow 2R_2-OOC-R_1 + Zn(OH)_2 \qquad \textbf{eq.2.1}$$

$$\mathrm{In(acac)_3} + 3\,R_2-OH \rightarrow 3\,acac-R_2 + In(OH)_3 \qquad \textbf{eq.2.2}$$

$$Zn(OH)_2 + In(OH)_3 \rightarrow Zn_{1-x}In_xO + H_2O \qquad \textbf{eq.2.3}$$

where R_1-COO refers to the carboxylate in $ZnSt_2$, R_2-OH refers to the DDOL, and the group III dopants use $In(acac)_3$ as an example.

2.2.2 Synthesis of Gallium Phosphide Nanowires

The chemical vapor deposition (CVD) method was used to synthesize gallium phosphide nanowires, based on the precursors GaP, Ga, and P. The metal catalyst, Au, was used in the experiment, which was deposited on a clean substrate. Si substrates within 1 cm^2 in area, which were washed with deionized water and ethanol, then dried in the nitrogen flow, were used as

holders to grow nanowires. All the reactants and catalyst were put onto a mica sheet on the top of an aluminum boat, then the boat was placed in the center of a horizontal two-inch diameter quartz gas flow tube inside a three-temperature-zone tube furnace (zone 2). Meanwhile, another aluminum boat, containing the growth substrate, was placed 25 cm downstream from the precursors (zone 3). The tube was evacuated to 0.1 Torr and then purged with high purity argon gas (100 sccm flow rate) under 200 Torr before the reaction started. The tube furnace was subsequently heated to the desired temperature under argon gas flow. For samples synthesized under hydrogen flow, after reaching the set temperature, hydrogen gas was purged in at the desired rate while argon flow rate was decreased to maintain the total gas flow rate of 200 sccm. The reaction sustained for 90 minutes, and the pressure was maintained at 200 Torr during the reaction. Samples were allowed to naturally cool down to room temperature under argon flow.

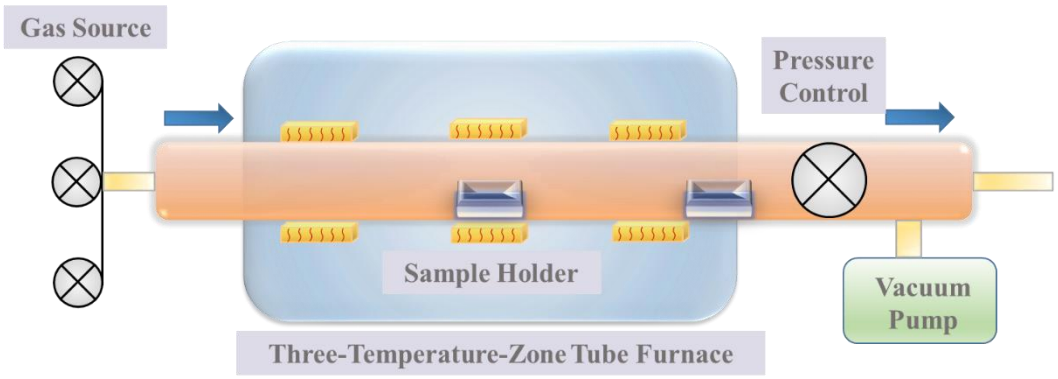

Figure 2.1 Illustration of a CVD reactor.

2.3 Characterization Techniques

2.3.1 Powder X-ray Diffraction (PXRD)

Powder XRD is applied to primarily identify the crystal structure of the semiconductor NCs and NWs. When an incident monochromatic X-ray beam hits the rotating sample, scattering will occur and undergo destructive and constructive interference which is the process of diffraction. A crystal structure such as the shape, size and arrangement information can then be obtained from the intensity and direction of the diffraction. Especially the size of the crystal can be obtained through the Scherrer equation[86]:

$$L_{hkl} = \frac{k\lambda}{B\cos\theta} \qquad \textbf{eq. 2.4}$$

L_{hkl} is the crystallite size in the scale of nm and *k* is the dimensionless shape factor approximately equal to 0.9, λ is the wavelength of the X-rays and B is the full width at half-maximum (FWHM) of the diffraction peak, θ is the diffraction angle in radians.

The measurement took place on an INEL XRD diffractometer, the source of X-rays is Cu $K_{\alpha 1}$ radiation with the wavelength of 1.5406 Å; samples are placed on an aluminum sample holder with the generator at 30 kV and 30 mA.

2.3.2 Scanning Electron Microscopy (SEM)

The typical morphology, composition, and yield of the NWs can be detected by SEM. A high energy electron beam is applied to scan the sample. By analyzing the secondary electrons, the image of the sample can be obtained. SEM is extremely sensitive to materials with a rough surface or uneven fractions, which makes it a powerful tool to study the surface morphologies of samples. For this research, the images were performed with LEO 1530 microscope with the

operating voltage of 10 kV, the output images are all collected using the secondary electron mode. Energy dispersive X-ray spectroscopy (EDX) is used to roughly analyze the elemental composition of the synthesized sample. The ability to distinguish elements is due to the characteristic X-ray energy for each element.

2.3.3 Transmission Electron Microscopy (TEM)

TEM provides images with precise morphology and structure information. An electron beam transmits through ultra-thin samples and collects information from the interior of the sample. By analyzing the electron diffraction pattern, species, structure and defect information can be obtained. In terms of TEM measurements, all related samples are usually diluted and sonicated in order to make them well distributed on the TEM copper grid with lacey Formvar/carbon support films. The TEM images were then obtained with a JEOL 2010F microscope operating at 200 kV. The atomic arrangement and inter-plane crystal spacing are further identified by selected area electron diffraction (SAED) and high-resolution TEM (HRTEM) using Gatan Digital Micrograph software.

2.3.4 Raman Spectroscopy

Raman spectroscopy is a powerful tool to characterize materials and detect vibrations modes based on the frequency shift of scattered laser photons. The vibrational properties can be related to the strength, length and the arrangement of the chemical bond.[87] It has a strong sensitivity to the composition of the investigated compounds and is sensitive to impurities and the presence of disorders. Raman scattering can interact with molecular vibrations. The interaction will then lead to a shift of the energy and give feedbacks of the vibrational modes. In Raman spectrometers, samples are illuminated by a laser beam. The corresponding electromagnetic radiation is collected

through a monochromator which is capable of filtering out the elastic Rayleigh scattering and send the remaining radiation to a detector. The Raman spectroscopy was performed at room temperature with a Renishaw 1000 spectrometer connected to a BH-2 Olympus microscope. The measurements were performed in a confocal configuration, and the samples were excited using the Millenia-pumped Tsunami laser (Spectra-Physics) emitting at 785 nm, the employed radiation source was 10 % of the total output power (40 mW). Before each measurement, the spectrometer will be calibrated using a silicon foil.

2.3.5 Ultraviolet-Visible-Near-Infrared(UV-Vis-NIR) Spectroscopy

UV-Vis-NIR spectroscopy provides the measurement of electronic absorption with an extensive range of wavelength. Moreover, the optical properties and the electronic structures of the materials within the measurement range such as the free carrier absorption and band gap transition can also be determined. A Varian Carey 5000 UV-Vis-NIR spectroscopy was used in this study to obtain the absorption spectra. Solid state UV-Vis-NIR absorption spectra were collected by drop-casting the colloidal solution on the quartz substrates to form a film so as to avoid the solvent effect in the NIR region. Typically a spectroscopy will collect from 200 nm to 3300 nm.

2.3.6 Fourier Transform Infrared (FTIR) Spectroscopy

FTIR spectroscopy can acquire optical properties of the materials in the infrared range on account of the frequencies of vibrations. The organic molecules on the surface of NCs can be recognized due to their different functional groups. Moreover, since doped semiconductor NCs

possess plasmonic properties in the MIR region, FTIR spectroscopy could be applied to identify these properties. The whole scene of the plasmonic properties of NCs could then be obtained by the combination of FTIR and the UV-Vis-NIR spectroscopy. In this study, all the FTIR spectra were collected through the KBr pellets in the range from 400 to 4000 cm^{-1} on the FTIR Bruker Tensor 37.

2.3.7 Magnetic Circular Dichroism (MCD)

In this study, MCD was measured using Jasco J-815 spectropolarimeter in a Faraday configuration and the samples were coated on the strain-free quartz substrate inside an Oxford SM 4000 magneto-optical cryostat. The field dependent MCD were realized under 5 K from 1 T to 7 T and temperature-dependent measurement of MCD was carried out at 7 T from 5 K to 300 K.

Chapter 3 Study of the Plasmonic and Magnetoplasmonic Properties of Indium-doped and Aluminum-doped ZnO (IZO and AZO) Nanocrystals

3.1 Crystal Structure of IZO and AZO NCs by XRD

The crystal structure of as-synthesized IZO NCs was confirmed by the XRD patterns with an In/Zn molar ratio up to 20 %, as shown in Figure 3.1 and Figure A1. At all doping levels, the XRD patterns are in good agreement with the reference pattern which is bulk ZnO in a wurtzite crystal structure. No diffraction peaks originating from secondary phases such as indium oxide (In_2O_3) or mixed oxide ($ZnIn_2O_4$), which often exist in the doped ZnO thin films, were detected.[88,89] The average particle sizes, calculated from the Scherrer equation, are estimated to be 12.0 nm for pure ZnO and 9.1±1.0 nm for all the doped samples with a slight decrease when increasing the doping concentration.

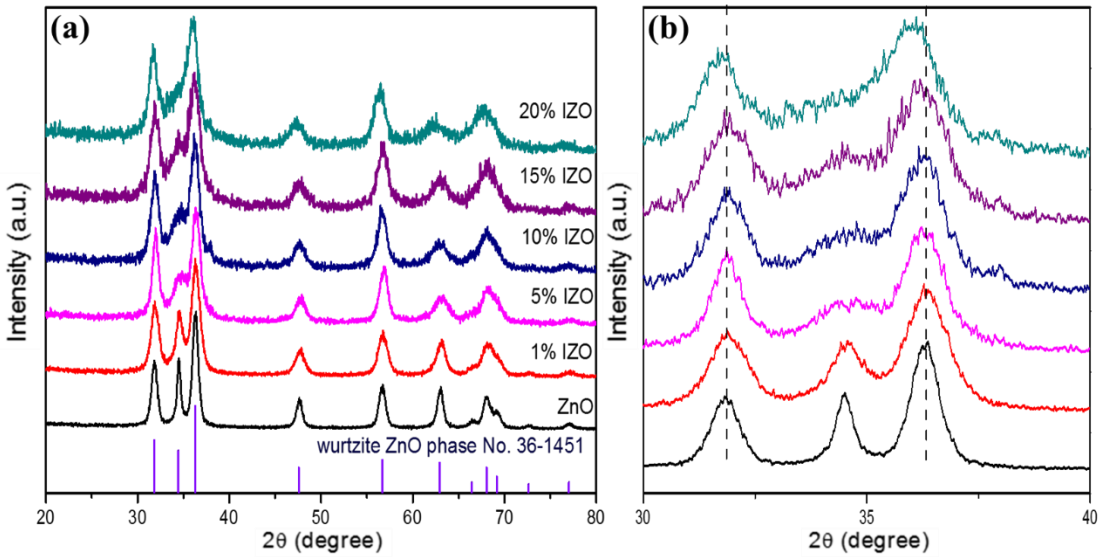

Figure 3.1 XRD pattern for IZO with different starting In/Zn molar ratio up to 20 %. Purple lines correspond to the XRD pattern of bulk wurtzite ZnO (JCPDS 36-1451).

As illustrated in Figure 3.1 (b), with an increase in doping concentration, the diffraction peaks for IZO samples tend to broaden slightly and shift to lower angles, compared to the pure ZnO sample. According to the Scherrer equation, the broad peak accounts for a decrease in the size of the NCs. These phenomena could arise from the increase of lattice strain in the nanoscale.[90] The In^{3+} dopant ions have a larger ionic radius than the Zn^{2+} ions, hence when In^{3+} ions doped into ZnO NCs, the lattice will expand and a tensile strain will appear. The space of planes is affected by the tensile strain in the lattice and result in changes in the crystal size and the reflection angle.

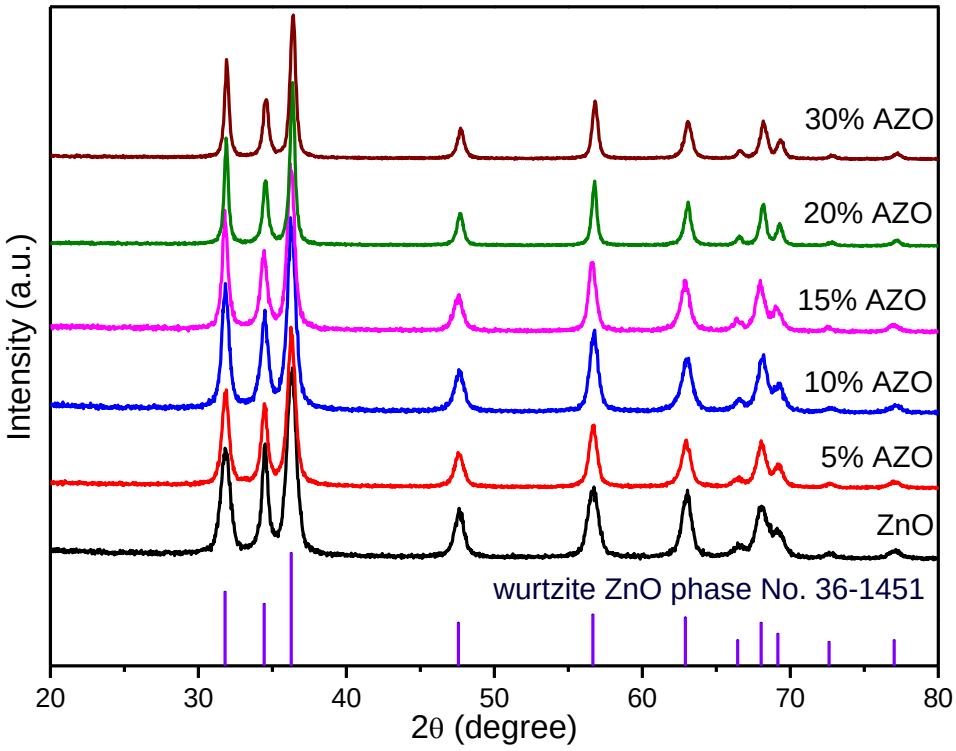

Figure 3.2 XRD pattern for AZO with different starting Al/Zn molar ratio up to 30 %. Purple lines correspond to the XRD pattern of bulk wurtzite ZnO (JCPDS 36-1451).

Figure 3.2 shows the crystal structure of synthesized AZO NCs by the XRD patterns. These samples have Al/Zn molar ratio varying from 5 % to 30 %. Similar to IZO NCs, all the AZO samples have the wurtzite crystal structure and are in accordance with the pattern of bulk ZnO. No diffraction peaks originating from aluminum oxide (Al_2O_3) or other impurities such as gahnite ($ZnAl_2O_4$) were detected. Also, no significant peak broadening or peak shift appear in AZO samples indicating that the actual doping concentration for all the samples is not as high as IZO samples. However, the calculated average particle sizes are 14.4±0.4 nm for low doping AZO samples (5 %, 10 %, and 15 %), and around 29.0 nm for highly doped samples (20 % and 30 %). The difference between low and high doping concentrations need to be further analyzed with the help of TEM.

3.2 Morphology of IZO and AZO NCs by TEM

Figure 3.3 and Figure 3.4 show the representative TEM images of 5% and 10% IZO NCs, respectively. It can be observed from the low-resolution TEM images in Figure 3.3 (a) and Figure 3.4 (a) that most of the IZO NCs have spherical or pseudo-spherical shapes. The high-resolution TEM images for a single NC exhibit the lattice spacing for IZO samples, which affirms the crystalline structure. For 5 % IZO NCs, the lattice spacing is around 2.9 Å, and for 10 % IZO NCs, the lattice spacing is around 2.8 Å. Both samples correspond to the (100) plane of bulk wurtzite ZnO. As represented in Figure 3.3 (d) and Figure 3.4 (d), the average particle size is 11.1±1.4 nm for 5 % IZO sample and 10.9±1.3 nm for 10 % IZO sample, respectively, which are in reasonable agreement with the calculated value form the XRD patterns using the Scherrer equation.

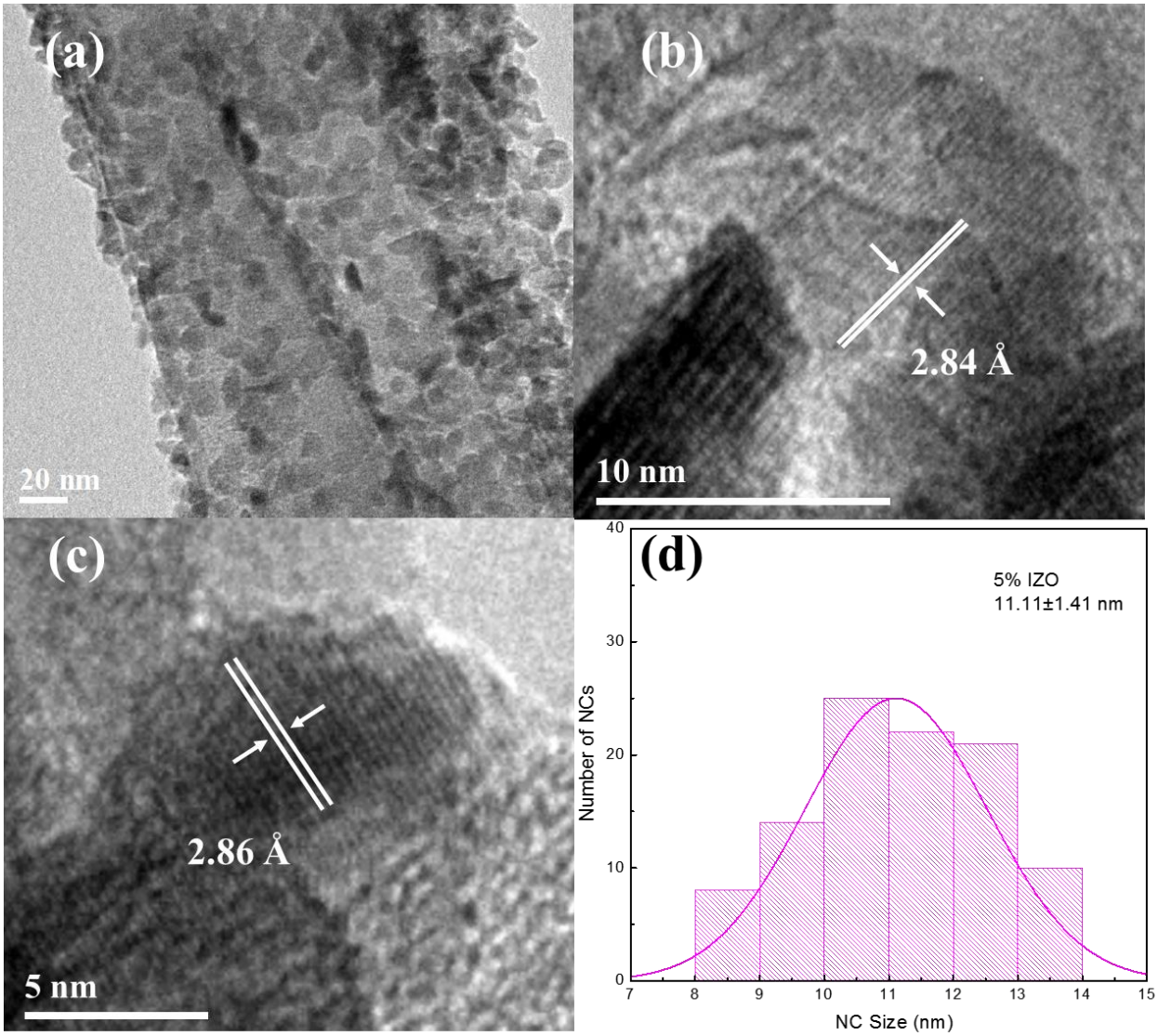

Figure 3.3 Representative TEM images of IZO NCs with the starting doping concentration of [In]/[Zn]=0.05. (a) Low-resolution overview TEM images of IZO NCs. (b) and (c) High-resolution TEM image of a single nanoparticle with measured lattice spacing. (d) The size distribution of IZO NCs.

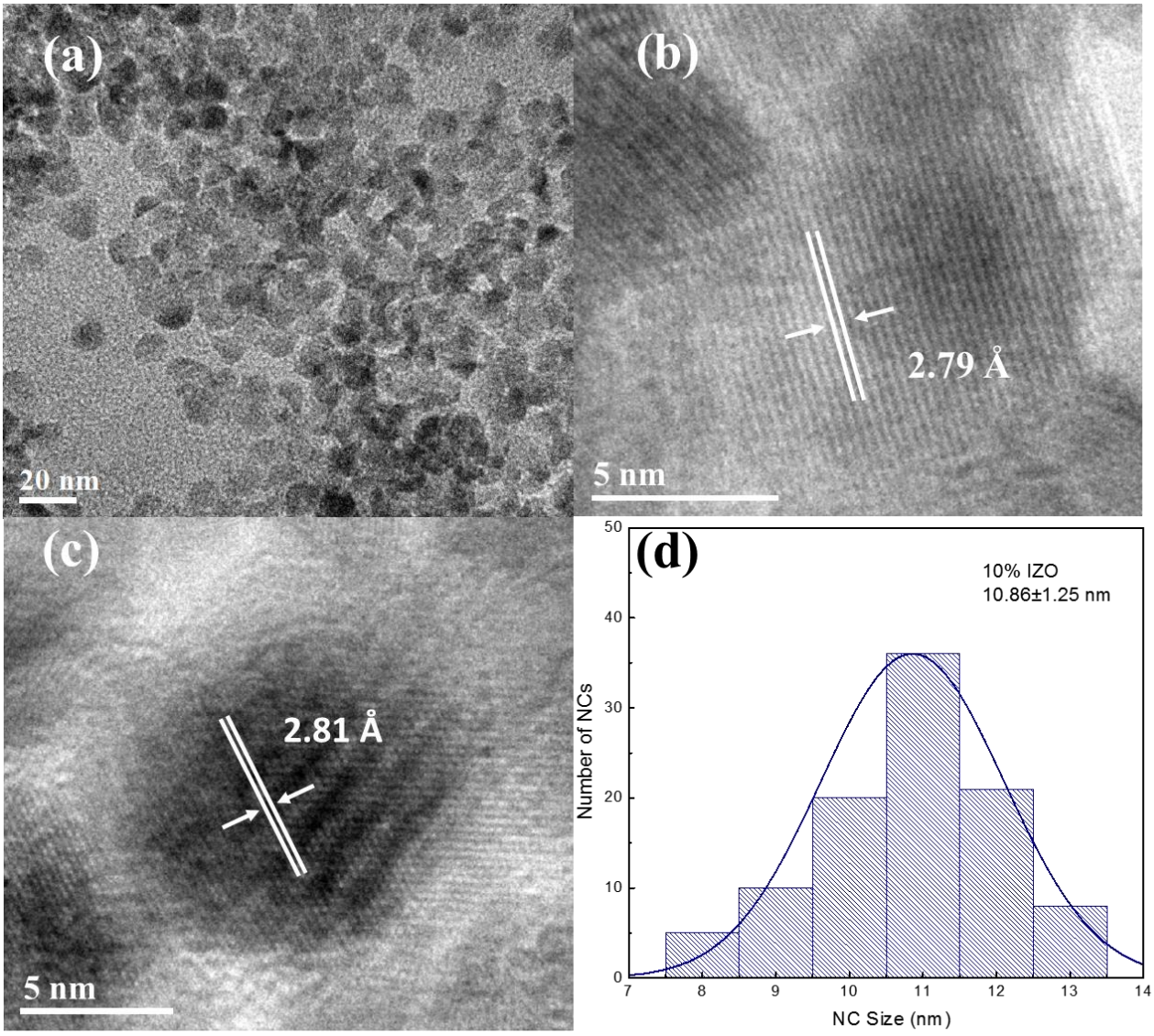

Figure 3.4 Representative TEM images of IZO NCs with the starting doping concentration of [In]/[Zn]=0.10. (a) Low-resolution overview TEM images of IZO NCs, (b) and (c) high- resolution TEM image of a single nanoparticle with measured lattice spacing and (d) the size distribution of IZO NCs.

The representative TEM image of 10 % AZO NCs is shown in Figure 3.5. The overview TEM image of 10 % AZO NCs in Figure 3.5 (a) shows that the NCs obtain spherical or elongated

shapes, and some of the particles may even have a pyramidal shape. This could happen since undoped ZnO NCs often own both elongated and spherical shapes.[91] The lattice spacing around 2.8Å for 10 % IZO NCs is obtained from high-resolution TEM images from Figure 3.5 (b) and (c), which consistent with the (100) plane of bulk wurtzite ZnO. Figure 3.5 (d) illustrates the particle size distribution around 14.6±1.2 nm, which is similar to the calculated value from XRD.

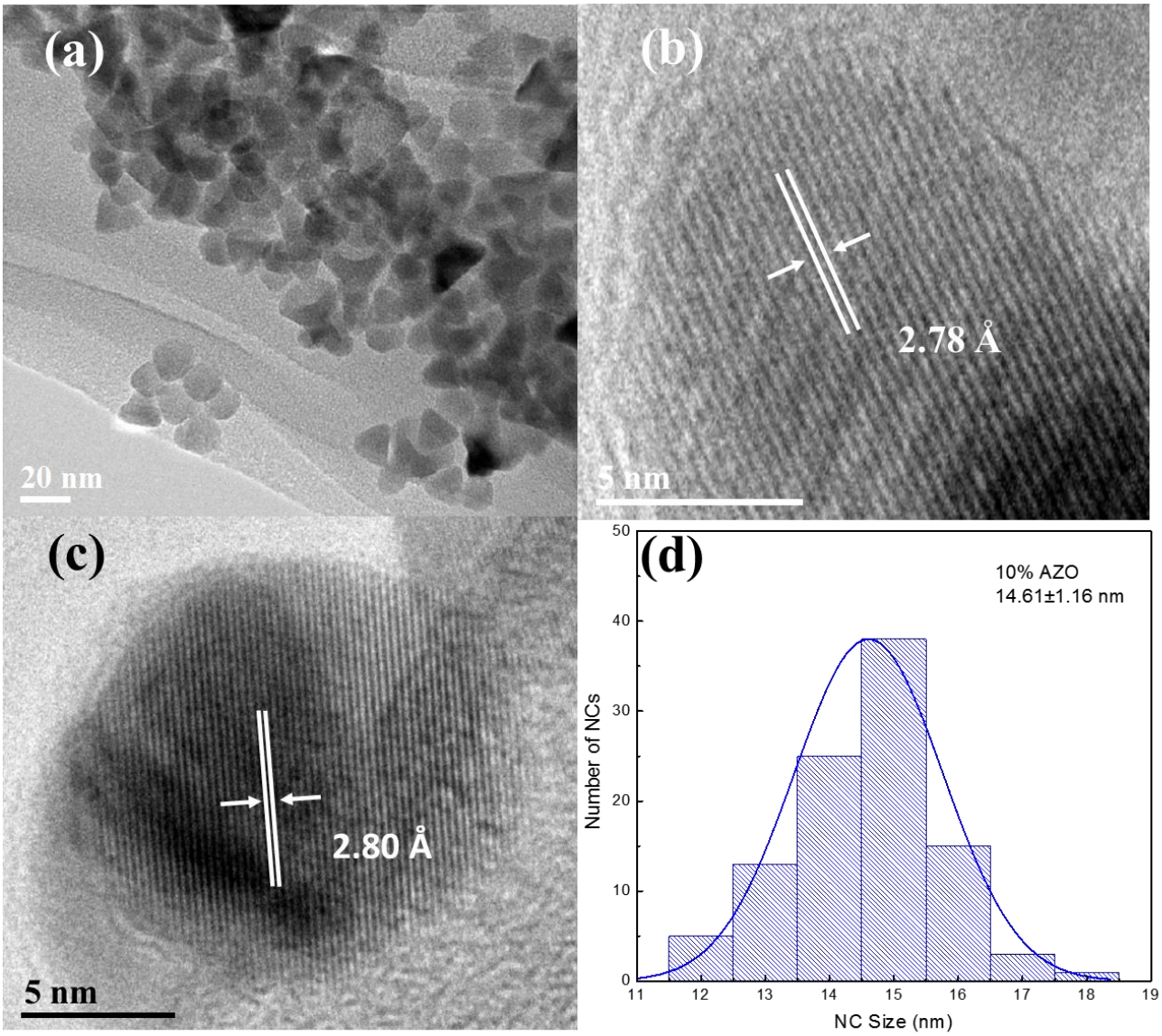

Figure 3.5 Representative TEM images of AZO NCs with the starting doping concentration of [Al]/[Zn]=0.10. (a) Low-resolution overview TEM images of AZO NCs, (b) and (c) high-resolution TEM image of a single nanoparticle with measured lattice spacing and (d) the size distribution of AZO NCs.

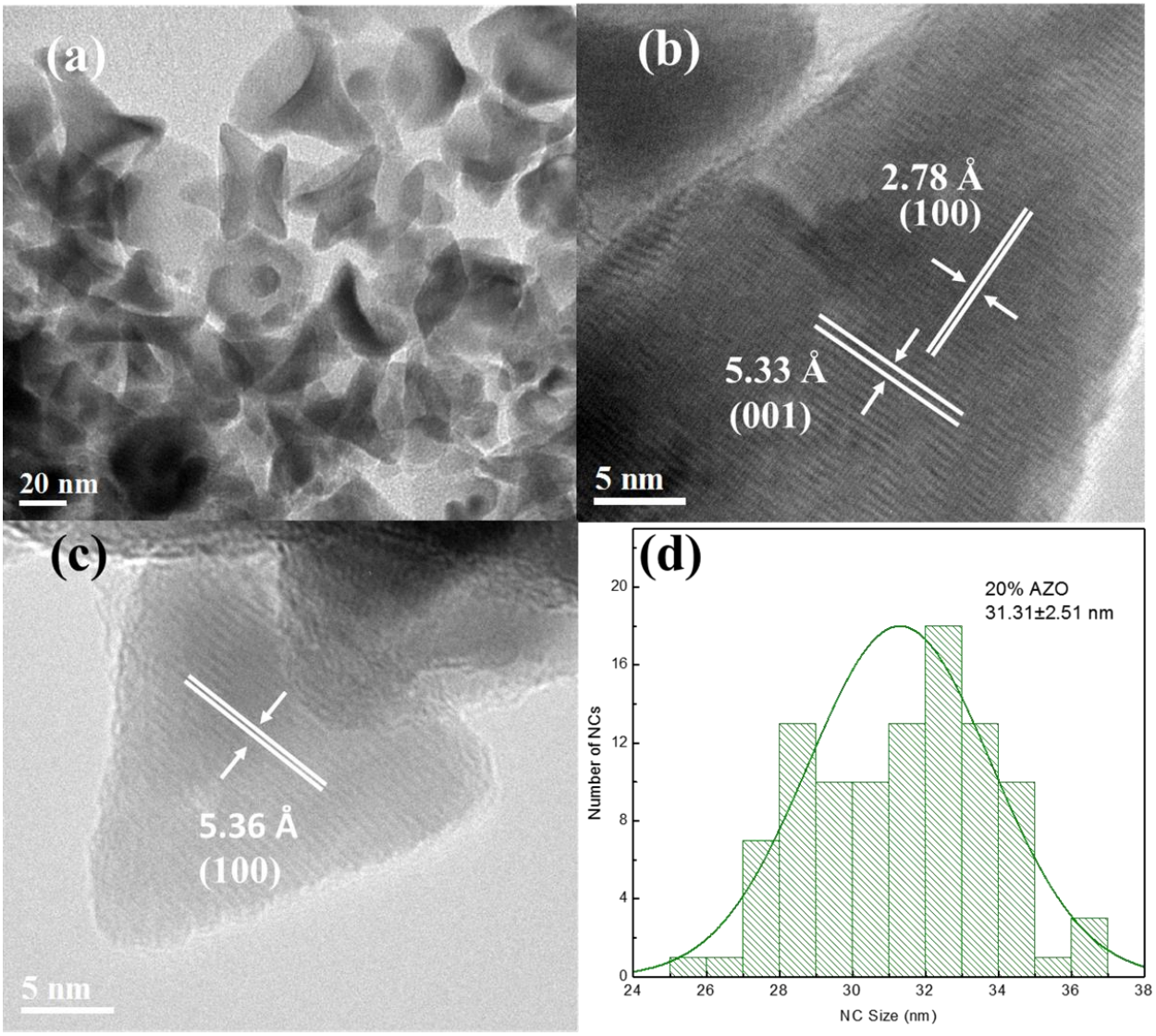

Figure 3.6 Representative TEM images of AZO NCs with the starting doping concentration of [Al]/[Zn]=0.20. (a) Low-resolution overview TEM images of AZO NCs, (b) and (c) high-resolution TEM image of a single nanoparticle with measured lattice spacing and (d) the size distribution of AZO NCs.

Figure 3.6 is the representative TEM image of 20 % AZO NCs. It should be noted that the shape of 20 % AZO NCs obtained from Figure 3.6 (a) has a pyramid or hexagonal pyramid morphology which is significantly different from the 10% AZO NCs. The change in morphology may be attributed to the existence of different crystal facets in 20 % AZO NCs and the difference in their growth velocities. The different planes formed on different surfaces can produce a permanent and spontaneous dipole moment which diverge the surface energy, and hence generate the pyramidal shape.[92] The different facets can be confirmed by the high-resolution TEM images in Figure 3.6 (b) and (c), which shows two different lattice spacings. The lattice spacing at 2.8 Å corresponds to the (100) plane similar to the 10 % AZO NCs, and the lattice spacing around 5.3 Å are assigned to the (001) plane. A relatively broad size distribution is obtained for the 20 % AZO NCs, which is 31.3±2.5 nm. This value is in accordance with the previously calculated one by the Scherrer equation and the change in shape of 10 % and 20 % AZO NCs explains the large difference in size between two samples.

Table 3.1 gives the actual doping concentration for both IZO and AZO NCs from the relative elemental EDX analysis. For IZO NCs, the actual doping concentration is very close to the starting In/Zn value, especially the 5 % IZO NCs, which have a high doping efficiency. However, for the AZO NCs, the actual doping concentration is merely less than 1 % for both samples. Different doping efficiency may attribute to the different ionic radii for the dopants and different kinetics during the NC growth.

Table 3.1 Actual doping concentration of IZO and AZO NCs from the TEM relative EDX

NCs Starting Concentration	Dopant Concentration
5 % IZO	5.23 %
10 % IZO	7.88 %
10 % AZO	0.18 %
20 % AZO	0.70 %

3.3 Spectroscopic Studies

3.3.1 UV-Vis-NIR Absorption Spectra

The UV-Vis-NIR absorption spectra were obtained from solid-state samples in the range from 200 nm to 3300 nm. Figure 3.7 and Figure A2 (a) show the UV-Vis-NIR absorption spectra of pure ZnO and IZO NCs with different doping concentrations up to 20 %. To make an effective comparison of plasmonic peaks for different doping concentrations, all the spectra were normalized based on the shoulder of the band gap absorption at around 300nm. The plasmon resonance absorption occurs in the NIR region for IZO NCs compared to pure ZnO NCs which shows very little absorption. It should be noted that in pure ZnO NCs, unpaired electrons exist in the oxygen-defective lattice which contributes to the fluctuation around 3000 nm. When increasing the doping concentration, the absorbance of the plasmon resonance of IZO NCs will increase, which indicate the increase of free carrier density due to the dopants. 10 % IZO sample shows the strongest absorption, which is the optimal plasmonic resonance. Starting from 12 % to 20 %, the absorbance of IZO NCs decrease with increasing doping concentration, which may be attributed to the trapping of In^{3+} ions or the scattering of free carriers.[93]

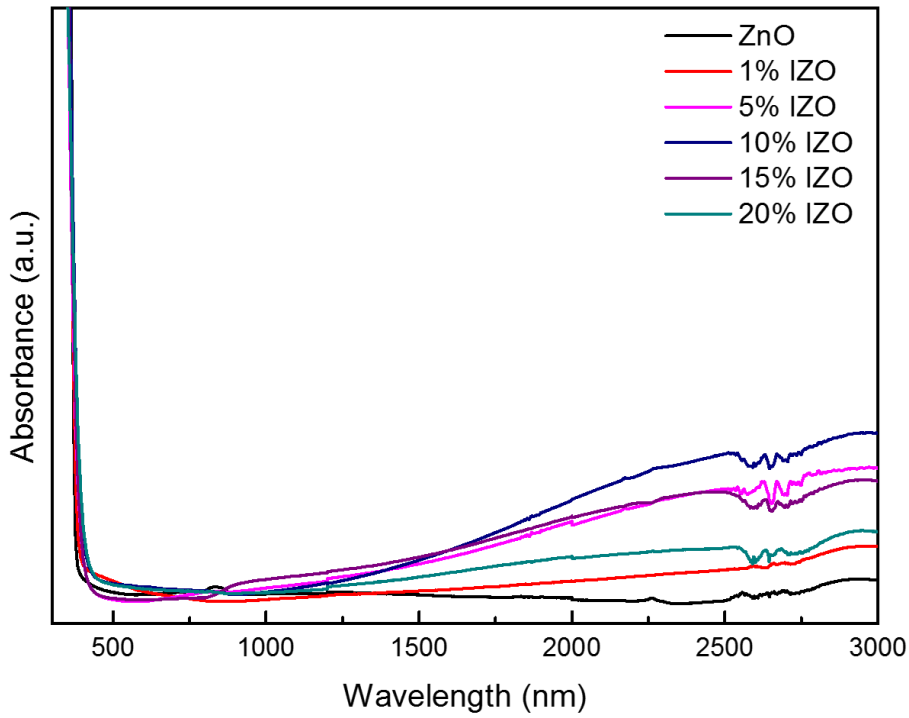

Figure 3.7 UV-Vis-NIR absorption spectra of pure ZnO and IZO NCs normalized at band gap absorption. The In/Zn ratio varies from 1 % to 20 %.

Based on the band gap absorption from UV-Vis-NIR spectra, the optical band gap for the ZnO and IZO NCs can be obtained from the Tauc plot. As shown in Figure 3.8 and Figure A2 (b), the band gap value for pure ZnO NCs is about 3.32 eV, which is in accordance with the reported value in literature.[46] The optical band gap of IZO NCs primarily shifts to higher energy with increasing doping concentration up to 10 % and then reduce to lower energy. It has the same trend for the NIR plasmon resonance absorption due to the variation of free carrier density, and this can be attributed to the Burstein-Moss effect.

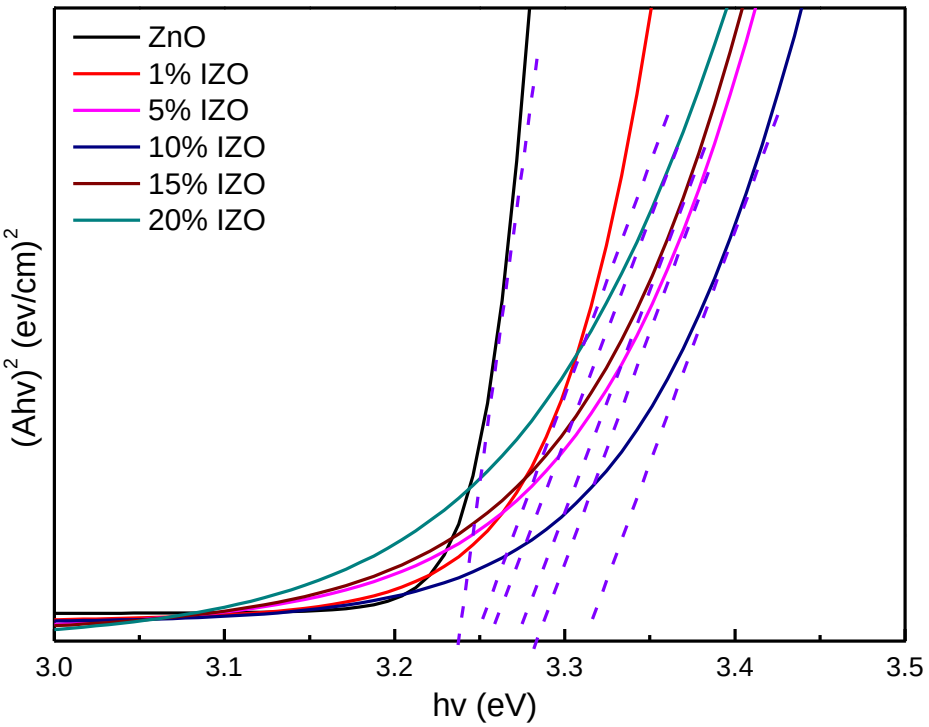

Figure 3.8 Tauc plots of the optical band gap of pure ZnO and IZO NCs with various doping concentration based on the UV-Vis-NIR spectra.

The band gap normalized UV-Vis-NIR absorption for AZO NCs from 5 % to 30 % is shown in Figure 3.9 (a). In the NIR, the plasmon resonance absorption of 5 % and 10 % are very weak due to the poor doping efficiency. An enhancement of the plasmonic peak occurs at around 3000 nm with increasing doping concentration. However, the absorption of AZO NCs is lower than that of IZO NCs, since the plasmon resonance for AZO mostly exists in the infrared region. Scattering starts to occur at 30 % AZO NCs in the UV-Vis region, hence no higher doping concentration is introduced in this study.

The optical band gap of AZO NCs for different doping concentration calculated from the UV-Vis-NIR spectra is shown in Figure 3.9 (b). From the Tauc plot, the band gap shifts to higher

energy with increasing doping concentration, which is in accordance with the increase of free carrier density due to the Burstein-Moss effect.

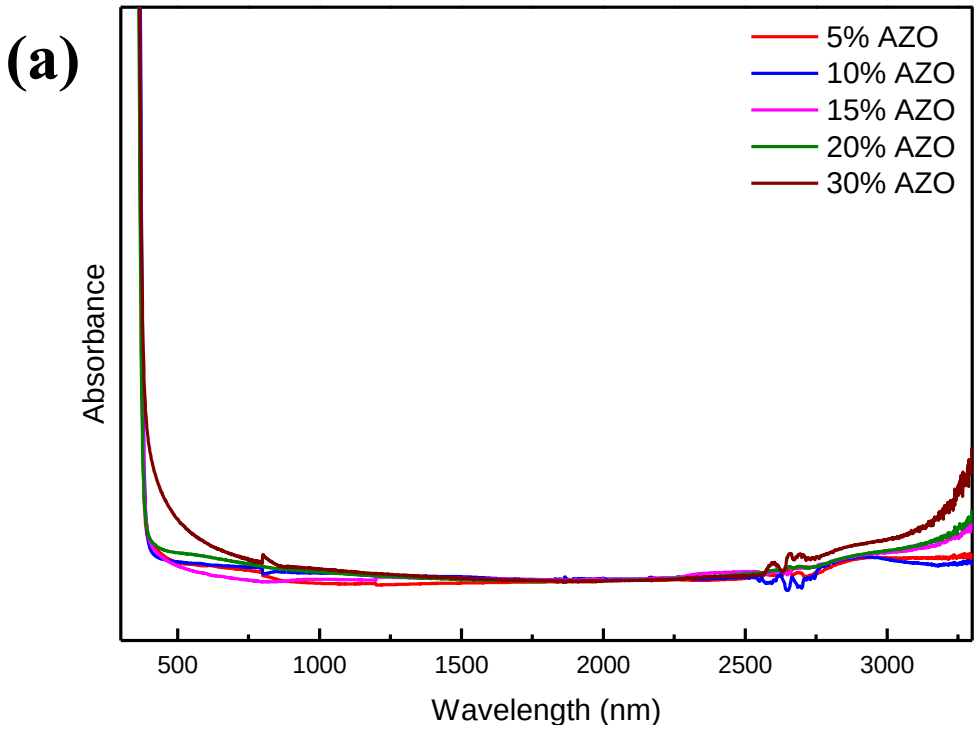

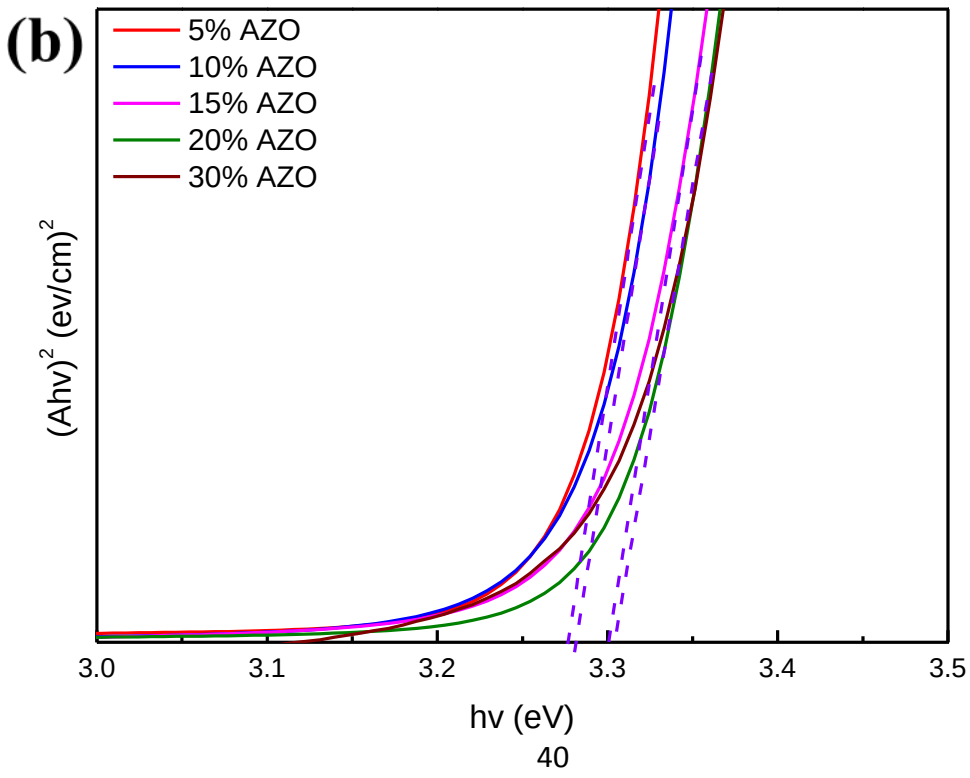

Figure 3.9 (a) UV-Vis-NIR absorption spectra of AZO NCs normalized at band gap absorption. The Al/Zn ratio various from 5 % to 30 %. (b) Tauc plot of the optical band gap of AZO NCs with various doping concentration based on the UV-Vis-NIR spectra.

3.3.2 FTIR Absorption Spectra

FTIR is another absorption technique which can characterize the plasmonic character for doped TCO NCs on account of the free electron oscillation. All the FTIR spectra were normalized using an empty KBr pellet. As illustrated in Figure 3.10, the representative normalized FTIR spectra for both pure ZnO and IZO NCs have two sharp bands at 2924 cm^{-1} and 2824 cm^{-1} which can be assigned to the CH_2 asymmetric and symmetric stretch of the solvent (OA) used in the synthesis step, respectively. Meanwhile, the two sharp peaks at 1566 cm^{-1} and 1467 cm^{-1} are the COO-band stretch formed during the reaction of host ions and dopants with DDOL, these two peaks also confirm the excellent solvent dispersibility.

For pure ZnO NCs, only a weak plasmon resonance exists due to partly delocalized free electrons in the oxygen-deficient lattice and the overall spectrum appears flat.[49] Nevertheless, similar to the UV-Vis-NIR spectra, with an increase of doping concentration for IZO NCs up to 10 %, the absorbance of a broad plasmon resonance peak increased monotonically. However, above 12 % the absorbance started to decrease with the increase of starting doping concentration. It can be observed that for IZO NCs, the maximum of the plasmonic peak is around 4000 cm^{-1}. The plasmon resonance peak in both the UV-Vis-NIR spectra and the FTIR spectra are incomplete. Hence it is necessary to combine these two spectra together to obtain a full band of plasmon resonance absorption.

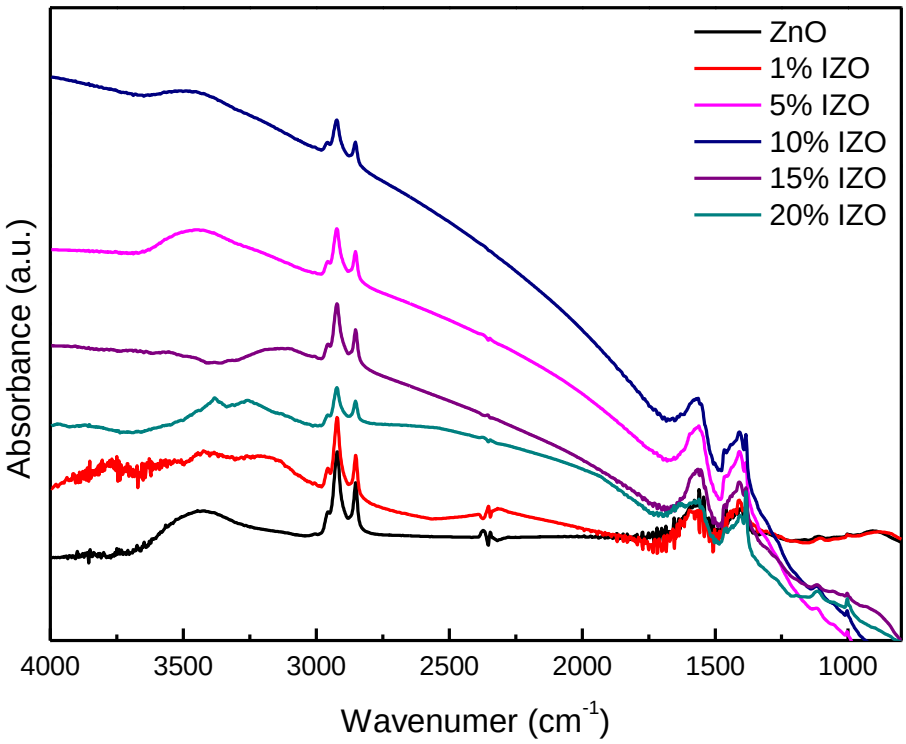

Figure 3.10 Normalized FTIR absorption spectra of pure ZnO and IZO NCs with different starting doping concentrations of In/Zn up to 20 %.

Figure 3.11 shows the normalized FTIR for AZO NCs at different starting doping concentration. In accordance with the IZO NCs, there are two sharp bands corresponding to the CH_2 stretch and two sharp bands from the COO- stretch. At low doping concentration (5 % and 10 %), it is indistinguishable to recognize the plasmonic resonance from the background. Nevertheless, at high doping concentrations (20 % and 30 %), an obvious broadband appears around 1000 cm^{-1}, which can be attributed to the plasmon resonance. It can be also observed that the plasmonic peak position for AZO NCs is significantly different with that of IZO NCs due to different charge carrier concentrations.

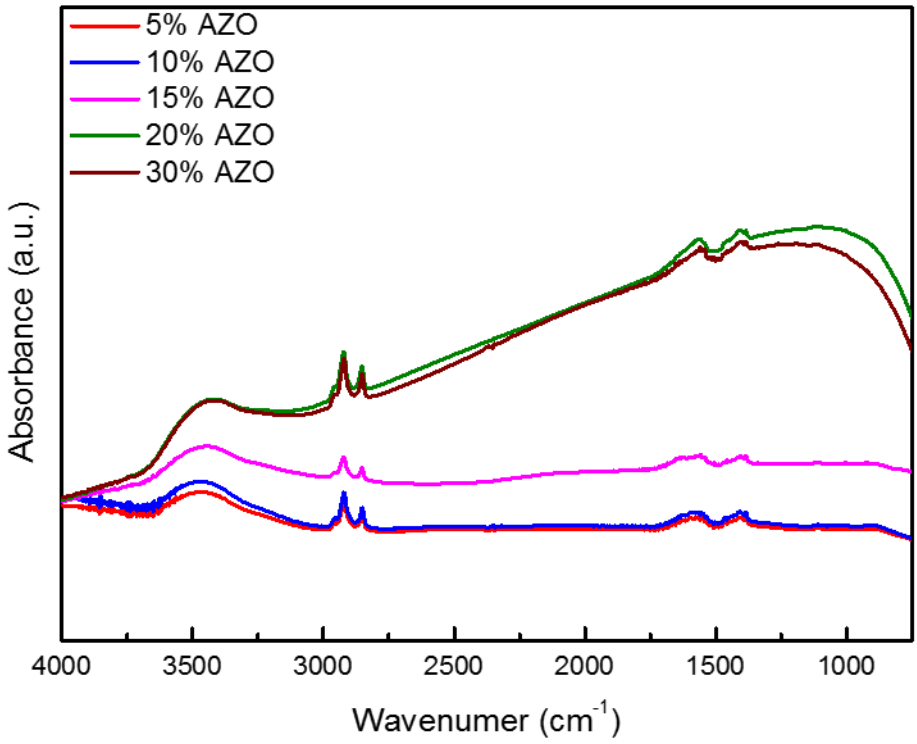

Figure 3.11 Normalized FTIR absorption spectra of AZO NCs with different starting doping concentrations of Al/Zn up to 30 %.

3.3.3 Combination of the Optical Absorption Spectra

The plasmonic peaks obtained from both the UV-Vis-NIR spectra and the FTIR spectra are incomplete, which makes it difficult to analyze the plasmonic properties, especially for the IZO NCs. Fortunately, because of the overlapping part of these two spectra in the region of absorption from 2500 nm to 3200 nm, it is possible to combine them to create a wide range optical spectrum from UV to the MIR region. The spectra for pure ZnO and IZO NCs are obtained from the spectra in Figure 3.7, Figure A2 (a) Figure 3.10, and Figure A2 (c). While the spectra for AZO NCs are the combination of Figure 3.9 (a) and Figure 3.11. To obtain reasonable spectra for the whole optical scope, the FTIR spectra are normalized based on the UV-Vis-NIR spectra. Completed

plasmon resonance absorbance can be acquired from the treated spectra for both IZO and AZO NCs.

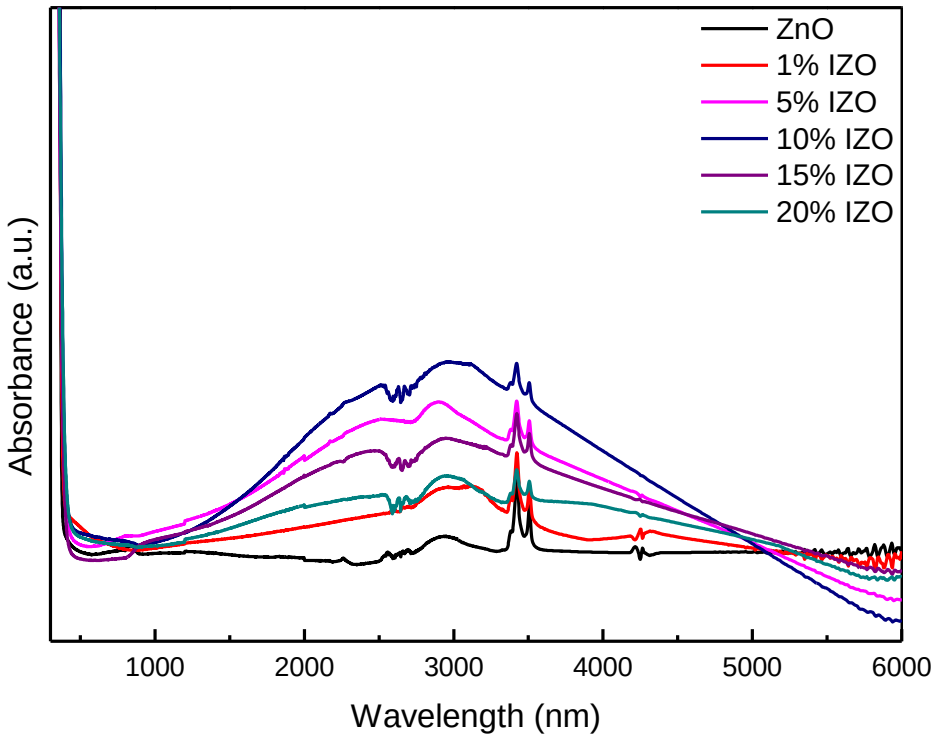

Figure 3.12 Normalized absorption spectra of pure ZnO and IZO NCs with different starting doping concentrations of In/Zn up to 20 %. The spectral range is from UV to the MIR by combining the UV-Vis-NIR spectra and the FTIR spectra.

As illustrated in Figure 3.12 and Figure A2 (d), pure ZnO NCs without dopants have a very weak plasmonic feature in the experimentally accessible optical region. A strong and broad plasmon resonance band can be observed for IZO NCs in various doping concentrations, indicating the plasmonic properties arising from the In^{3+} dopants. The optimized strongest plasmon absorption appears in the 10 % IZO NCs which is in agreement with the previous analysis. However, since the plasmonic peak around 3000 nm is located in the joining region of two different

spectra, it is difficult to observe the peak shift for different doping concentrations. For the 10 % IZO NCs, the free carrier density can be calculated using the Drude equation, which is 1.5 $\times 10^{20}$ cm^{-3}. This value approaches the value obtained from the literature. [50,90]

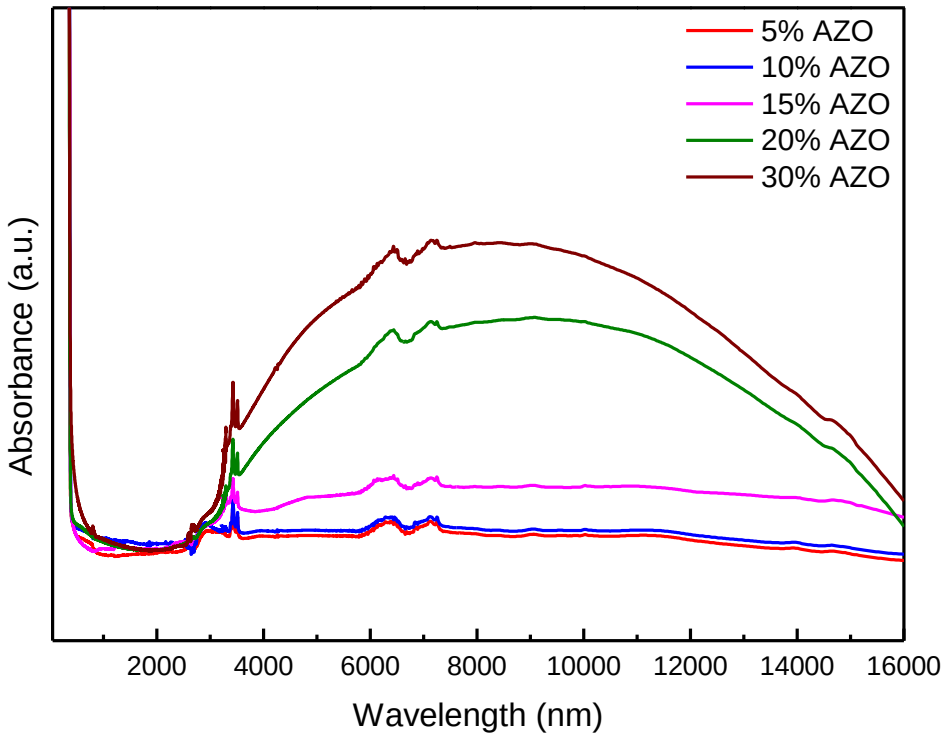

Figure 3.13 Normalized absorption spectra of AZO NCs with different starting doping concentrations of Al/Zn up to 30 %. The spectral range is from UV to the MIR by combining the UV-Vis-NIR spectra and the FTIR spectra.

Figure 3.13 demonstrates the entire normalized optical spectra of AZO NCs with starting doping concentration from 5 % to 30 %. Similar to the previous results, the plasmon resonance band intensity increases with increasing the doping concentration. Because of the low doping efficiency, it is difficult to observe the plasmon resonance band from the 5 % and 10 % AZO NCs, while 15 % AZO NCs begins to show a broadband in the optical region. Clear and strong plasmonic

bands appear in the spectra for 20 % and 30 % AZO NCs. An obvious blue shift could be observed as increasing the doping concentration, which confirms the increasing of free carrier density by increasing Al^{3+} dopants. The carrier density calculated using the Drude equation is 1.6×10^{19} cm^{-3} and 1.9×10^{19} cm^{-3} for 20 % and 30 % AZO NCs, respectively, which is in a reasonable range for doped TCOs.

3.4 Magneto-Optical Properties from MCD Spectra

MCD spectra of LSPR due to the cyclotron motion of free electrons upon the excitation of left and right circularly polarized light under external magnetic field have been observed for different plasmonic materials.[40,43] The key features of reported spectra are the linear magnetic field-dependent and temperature-independent MCD intensity which could be explained by the classical description of the cyclotron magnetoplasmonic modes.[40] In this study, the MCD spectroscopy was performed in Faraday configuration to examine the excitonic properties of plasmonic IZO and AZO NCs.

Figure 3.14 (a) and (b) show the absorption spectrum collected at 5K and MCD spectra collected under various magnetic field around the band gap region of 10 % IZO NCs whose actual doping concentration is 7.9 %. The MCD spectra show a strong negative band which coincides with the band edge absorption of the IZO NCs indicating the complete polarization of free carriers. In addition, the intensity of MCD band maximum at 3.36 eV has a linear relationship with the magnetic field as shown in Figure 3.14 (c). Furthermore, Figure 3.14 (d) suggests the MCD band intensity remains unchanged as temperature increases from 5 to 300 K. As reported in the previous

work from our group[94], the splitting of the excitonic transition has the same behavior as the MCD features of LSPR in the plasmonic II-VI ZnO NCs confirming the generality of the coupling between the exciton and plasmon in different plasmonic materials.

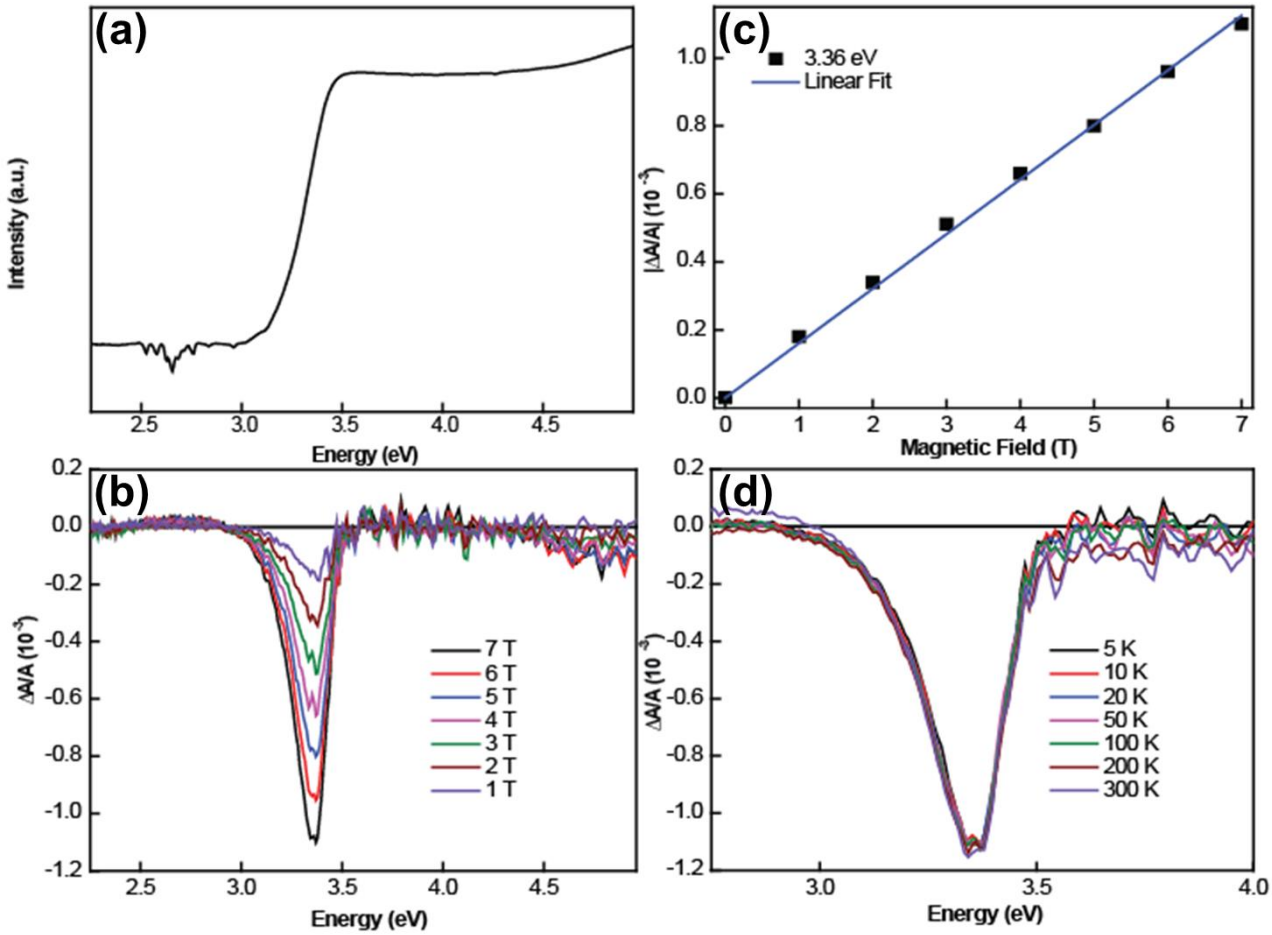

Figure 3.14 (a) Absorption spectra and (b) MCD spectra of 10 % IZO NCs collected at 5 K. MCD spectra collected at different external magnetic field strengths are indicated in the graph. (c) Magnetic field dependence of MCD intensity at 3.36 eV for ZnO NCs in (b) as a function of external magnetic fields. Blue solid trace is the linear fitting of the data points. (d) MCD spectra of pure ZnO NCs in (a) collected at 7 T for various temperatures (5 K – 300 K).

The negative singular sign of the MCD signal is a direct evidence of plasmon-induced carrier polarization. Meanwhile, the control experiments for pure ZnO involving localized conduction band electrons from previous work show no signal at room temperature.[95] Also, they follow Curie-type behavior characteristic for unpaired electrons. As the excitonic transition is off resonance with the LSPR of ZnO NCs, it is difficult to rationalize the explanation based on the direct coupling between plasmon and exciton. The mechanism of the plasmon-exciton coupling is more likely to involve a phonon-mediated process since both plasmon-phonon coupling and plasmon-exciton coupling are widely observed and well understood for different semiconductor materials.[96-98] More importantly, phonon could also transfer the angular momentum allowing for both generations of magnetoplasmonic modes and the splitting of the semiconductor band states. The experimental results of this study show more evidence towards the idea of phonon-mediated plasmon-exciton coupling. As shown in Figure A3 and A4, the MCD band maximum shifted to a lower energy with the increasing temperature which is consistent with the shift of absorption spectrum collected at the same time. The shift of excitonic transition of semiconductors with the change of temperature can be attributed to the temperature-dependent electron-phonon interactions which have been known for a very long time and observed with different semiconductors.[99] More interestingly, as the MCD band maximum shifts to lower energy, the intensity of band maximum slightly increases with increasing temperature. One of the possible reasons for this observation could be the slight increase of the angular momentum transfer rate in phonon-exciton interaction with increasing temperature.[94] Given that the relatively strong phonon-exciton interaction in NCs, the slight increase of angular momentum transfer rate could lead to the enhancement of the plasmon-exciton coupling strength which results in the increase in the MCD band intensity. In addition, as shown in Figure 3.17, the MCD intensity behaves similarly to the rate of angular

momentum transfer.[98] It is noticeable that this effect is not as pronounced in 10 % IZO NCs, which could be correlated to the weakening of the phonon-exciton interaction due to the large degree of local lattice distortion as evidenced by the negligible shift of the excitonic absorption as well as the MCD band.

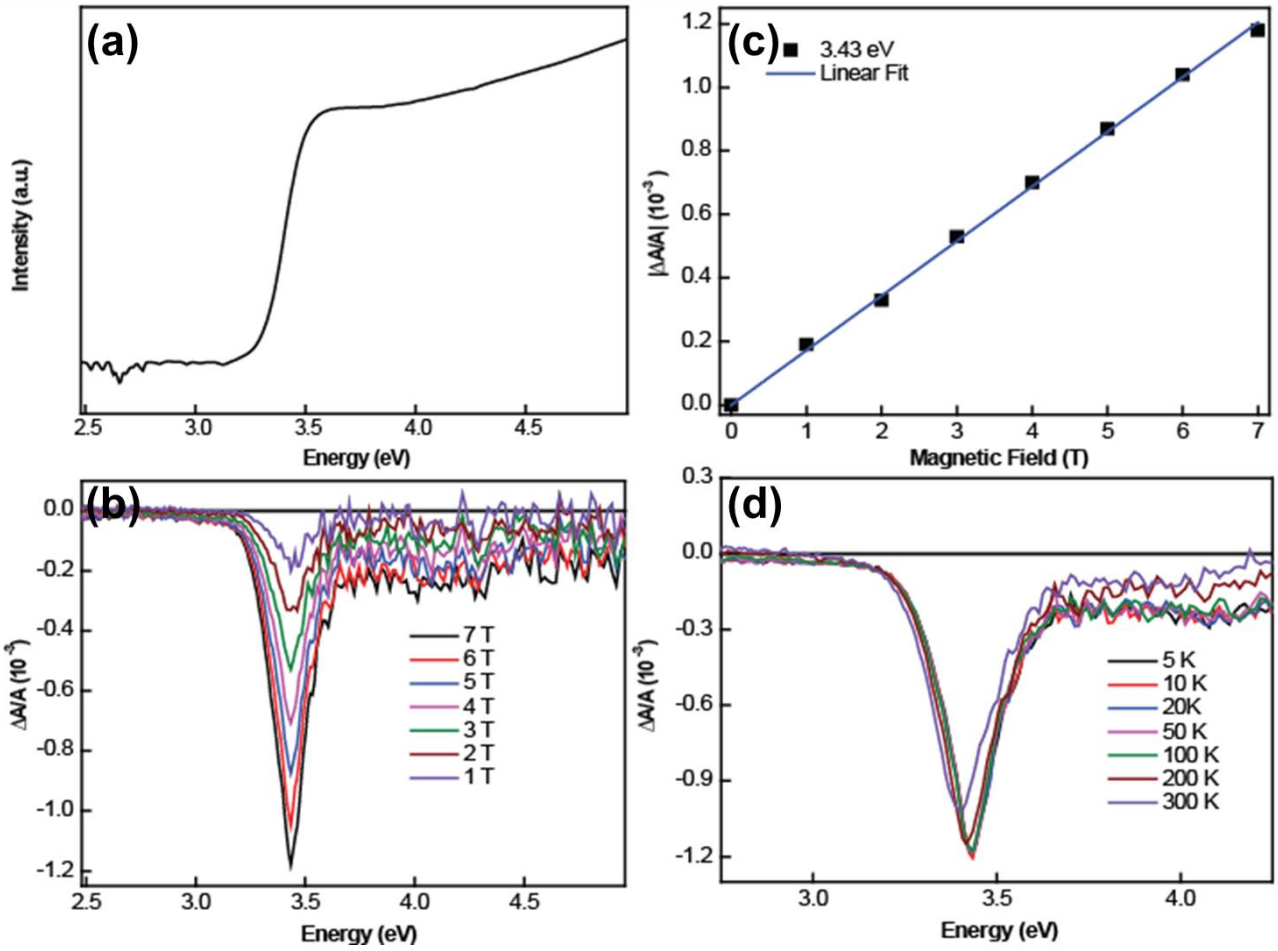

Figure 3.15 (a) Absorption spectra and (b) MCD spectra of 20 % AZO NCs collected at 5 K. MCD spectra collected at different external magnetic field strengths are indicated in the graph. (c) Magnetic field dependence of MCD intensity at 3.43 eV for ZnO NCs in (b) as a function of external magnetic fields. Blue solid trace is the linear fitting of the data points. (d) MCD spectra of pure ZnO NCs in (a) collected at 7 T for various temperatures (5 K – 300 K).

For 20 % AZO NCs (actual doping concentration: 0.7 %) MCD spectra, the negative MCD band was also observed with the band maximum intensity changing linearly to the applied magnetic field as indicated in Figure 3.15 (b) and (c). This could also be associated with the cyclotron magnetoplasmonic oscillations as a collective property of free electrons. However, as shown in Figure 3.17, the MCD band maximum has a slight decrease as the temperature increases which is contrary to the temperature-dependence of MCD band intensity observed for IZO NCs. The decrease of MCD band intensity at high temperature (greater than 100K) could possibly be related to the weakening of the plasmon-phonon coupling strength.

Surprisingly, similar features were observed in the MCD results of pure ZnO NCs synthesized under the identical experimental conditions. The non-zero MCD band intensity at 300K resembles the collective effect of the delocalized free electrons in the oxygen-defective ZnO lattice. The generation of a sufficient number of delocalized free electrons in intrinsic oxygen defective ZnONCs was also reported in the literature.[49] As for the temperature-dependence of the MCD band, compared to that of the AZO NCs, the intensity quickly decreases as temperature increases from 5 to 100 K, which could be related to the Curie-type paramagnetism induced by the localized nature of electrons associated with oxygen vacancy sites. Further decline of the MCD band intensity from 100 to 300 K, is likely to be related to the reduced plasmon-phonon coupling due to the weak oscillator strength of the plasmon oscillations, similarly to AZO NCs.

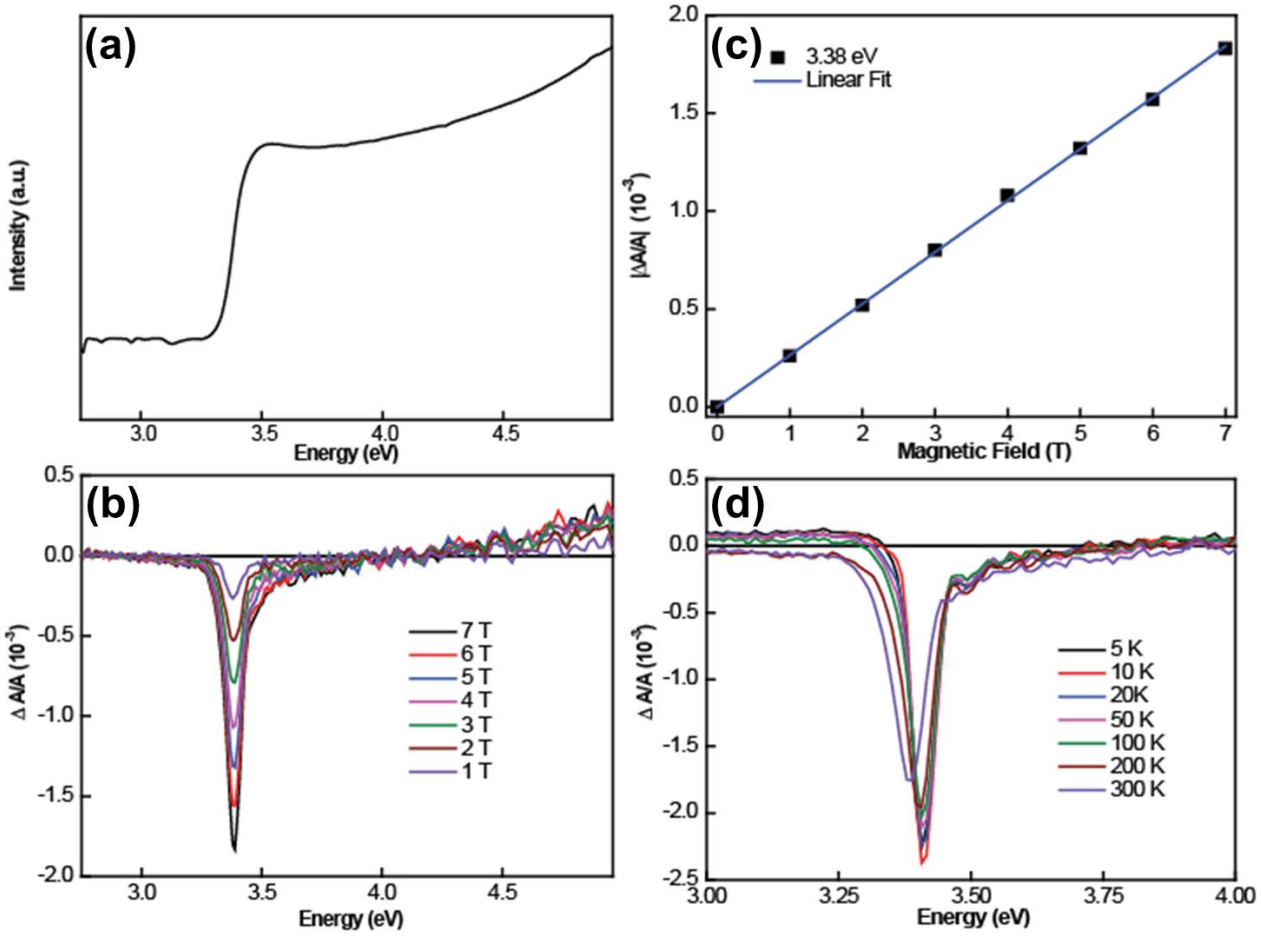

Figure 3.16 (a) Absorption spectra and (b) MCD spectra of pure ZnO NCs collected at 5 K. MCD spectra collected at different external magnetic field strengths are indicated in the graph. (c) Magnetic field dependence of MCD intensity at 3.38 eV for ZnO NCs in (b) as a function of external magnetic fields. Blue solid trace is the linear fitting of the data points. (d) MCD spectra of pure ZnO NCs in (a) collected at 7 T for various temperatures (5 K – 300 K).

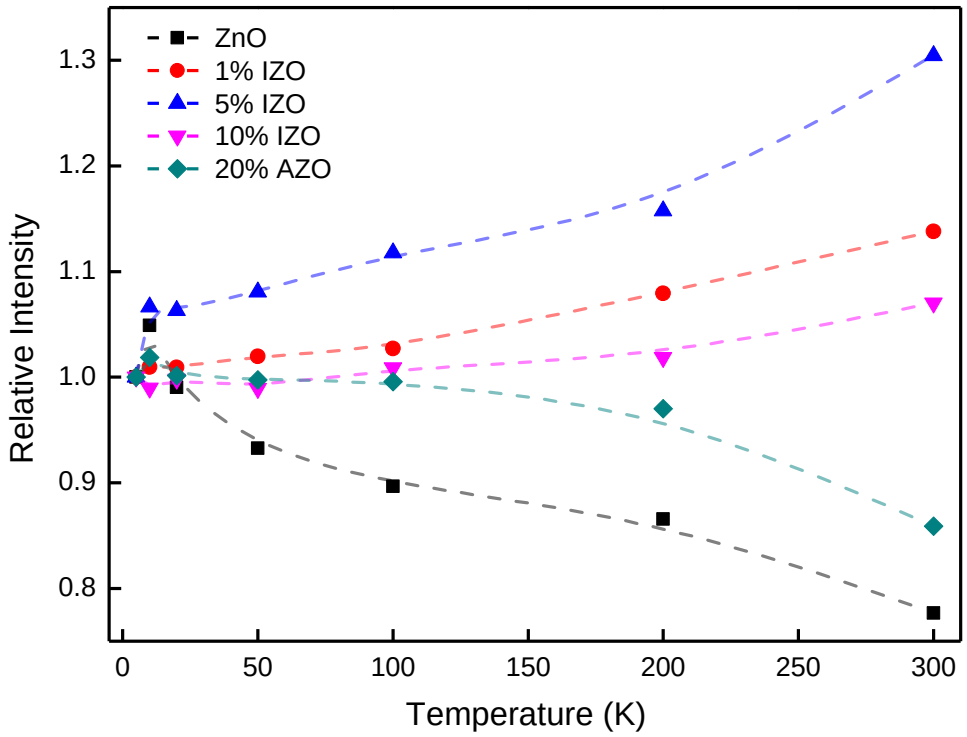

Figure 3.17 Temperature dependence of MCD relative intensity recorded at the maximum intensity of each temperature for pure ZnO, IZO (1 %, 5 %, 10 %), and AZO (20 %) NCs. The maximum intensities at 5 K for all the NCs are set as 1.

3.5 Conclusion

In conclusion, the indium and aluminum doped zinc oxide NCs with various doping concentrations have been successfully synthesized. The wurtzite crystal structure has been confirmed by XRD with no secondary phases detected for all samples. A uniform shape and high doping efficiency for IZO NCs have been demonstrated with TEM images and relative elemental EDX analysis. However, TEM images for AZO NCs show diverse shapes at different doping concentrations due to the existence of different growth facets at higher doping concentration which

contribute to the size deviations of NCs. The actual doping concentrations for AZO NCs are generally lower as 20 % AZO has an actual doping concentration less than 1 %.

UV-Vis-NIR spectra and FTIR spectra both confirm the existence of the plasmonic property of IZO and AZO NCs. With a proper combination of these two spectra, the integrated plasmon band was obtained. The peak positions are around 3000 nm for IZO NCs and around 8000 nm for AZO NCs. The highest plasmon band absorption has been obtained from the 10 % IZO NCs. Further increase in the In/Zn ratio reduces the plasmon band absorption due to the trap of In^{3+} ions. While in AZO NCs, the band absorption continues to increase due to the poor doping efficiency. The blue shift of the band gap for AZO NCs can be explained by the Burstein-Moss effect. The MCD spectra demonstrate for the first time exciton-magnetoplasmonic coupling in II-VI NCs, which gives rise to the band state splitting and carrier polarization. In this thesis, it tentatively proposed the role of phonon mediation in this plasmon-induced carrier polarization. A deeper understanding of this intriguing phenomenon requires additional experimental work and theoretical modeling.

Chapter 4 Control of the Spontaneous Formation of Oxide Overlayers on GaP Nanowires

4.1 Crystal Structure and Morphology of GaP NWs under Normal Growth Condition

The initial synthesis was performed in the excess of Ga, with Ga:GaP flux ratio of 1:1, at 1000ºC as described in section 2.2.2. The crystal structure of the NWs was performed by powder XRD as illustrated in Figure 4.1. It can be observed that the NWs exist in the zinc blende GaP (red lines) crystal structure. The diffraction peaks at 28º, 33º, 47º, 56º, and 59º, correspond to the (111), (200), (220), (311), and (222) lattice plane, respectively. While other remaining peaks indicate the characteristic for β-Ga_2O_3 (blue lines) structure. Given the amorphous nature of the NW shell, the β-Ga_2O_3 reflections suggest that the particles co-deposited on the growth substrate consist of crystalline Ga_2O_3.

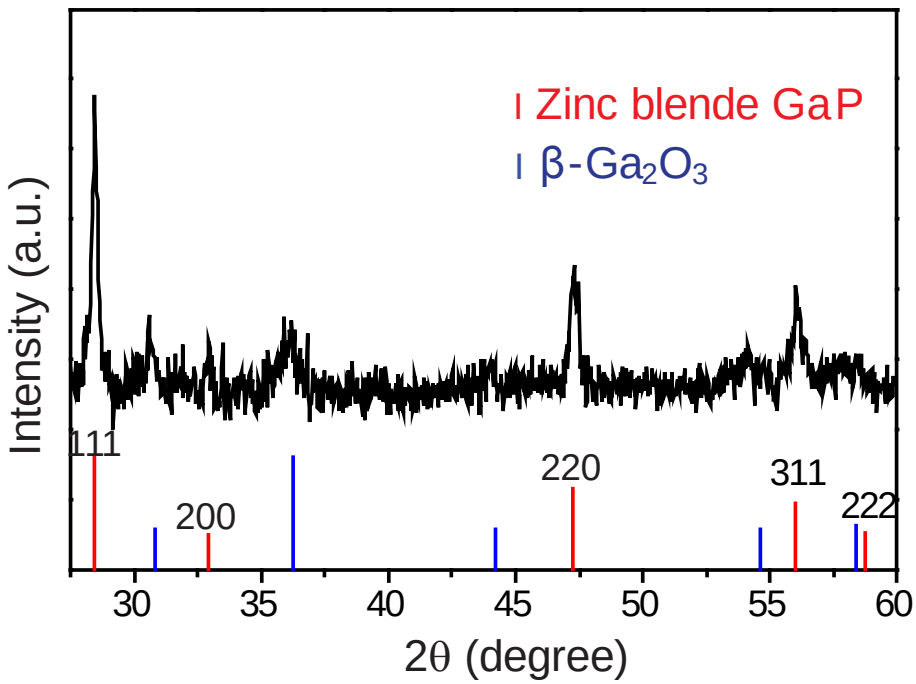

Figure 4.1 XRD pattern of NWs on the growth substrate synthesized at 1000 ^{o}C in argon flow with excess Ga (flux ratio Ga:GaP = 1:1). Red lines and blue lines correspond to the XRD pattern of bulk zinc blende GaP (JCPDS 12-0191) and β-Ga_2O_3 (JCPDS 020-0462), respectively.

Figure 4.2 (a) shows the overall SEM image of the NWs. It can be observed that the resulting product consists of a mixture of very long and curved NWs and large particles evenly distributed throughout the growth substrate. The average NW length is well over 5 μm. Figure 4.2 (b) shows a TEM image of a typical NW from this sample. The NW has an uneven surface with occasionally large protuberances along the growth direction. Selected area electron diffraction (SAED) pattern (inset in Fig. 4.2 (b)) indicates that the NW grows along <111> direction, which has been confirmed for other NWs in the sample. Figure 4.2 (c) shows a high-resolution TEM image of the same NW. The lattice spacing of 3.14 Å confirms the <111> growth direction, which is in accordance with the most intense peak in XRD result and is consistent with that of ZB crystal structure. Importantly, the NW has a thick outer layer which appears to be largely amorphous. The thickness of this layer ranges from 5 to over 20 nm, which can also be observed in Figure 4.2 (b) as the difference in contrast between the NW core and the outer shell layer along the NW. Elemental EDX analysis of the NW shows a significant amount of oxygen (Figure 4.2 (d)), which is consistent with the previously reported conclusions that the shell is made of native oxide.[77,80] Taken together, the results in Figure 4.1 and Figure 4.2 demonstrate the propensity of oxide formation in the process of GaP NW growth by CVD based on thermal evaporation of bulk semiconductor.

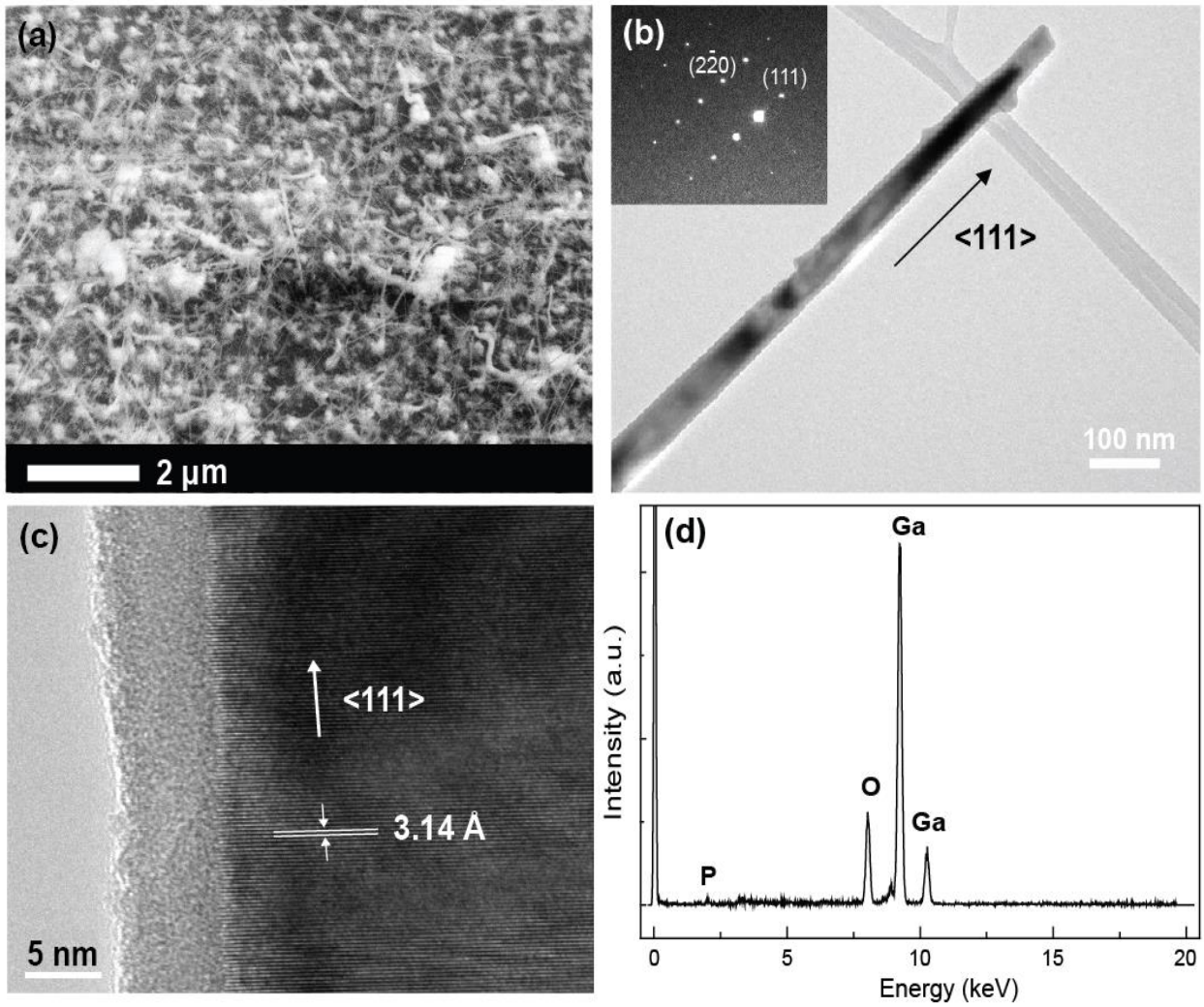

Figure 4.2 (a) SEM image of GaP NWs synthesized at 1000 °C in argon flow with excess Ga (flux ratio Ga:GaP=1:1). (b) Typical TEM image and corresponding SAED pattern (inset) of a single NW in (a). The arrow indicates the NW growth direction. (c) Lattice-resolved TEM image of the NW in (b). The average lattice spacing indicated in the image is consistent with <111> growth direction. (d) EDX spectrum of the NW in (b).

4.2 Influence of Hydrogen Flow on the NW Growth

In analogy to the growth of GaN NWs [56,79], it can be hypothesized that the synthesis of GaP NWs in reducing conditions could minimize the effect of residual oxygen and the probability of oxide shell formation. Figure 4.3 a-c shows SEM images of the samples grown at 1050 °C with Ga:GaP flux ratio of 1, but with different hydrogen flow. The sample grown in the absence of hydrogen (Figure 4.3(a)) appears nearly identical to that shown in Figure 4.2 (a), as expected. A relatively moderate hydrogen flow (50 sccm) leads to a significant decrease in the amount of co-deposited particles, although the NWs still have uneven surfaces or neckless-like structure with periodically spaced bumps along the NW (Figure 4.3 (b) and Figure B1 in Appendix B)[77,80]. These bumps are found to be amorphous and oxygen-rich, indicating that native oxide overlayers are still formed during NW growth. Further increase in the hydrogen flow rate (Figure 4.3 (c)) results in long and straight NWs with uniform thickness and smooth surfaces, as well as the nearly complete elimination of co-deposited crystalline Ga_2O_3 domains on the growth substrate. The SEM images in Figure 4.3 a-c illustrate the evolution of NW morphology in the flow of hydrogen as a reducing agent. The NW composition (Ga/P atomic ratio and the amount of oxygen) determined by EDX measurements of individual NWs from the samples synthesized with different H_2 flow rates are summarized in Figure 4.3 (d). While the Ga/P atomic ratio gradually decreases with increasing H_2 flow rate, the amount of oxygen initially increases followed by a sharp decrease. The initial increase in the amount of oxygen is likely due to the neckless-like morphology of NWs at moderate H_2 flow, where the bumps contain a large concentration of oxygen, despite the overall decrease in

the amount of co-deposited Ga_2O_3. Elimination of these bumps and the subsequent formation of straight and long NWs with smooth surfaces leads to a decrease in the amount of oxygen below 10 atom %, with the Ga:P ratio of ca. 1.2.

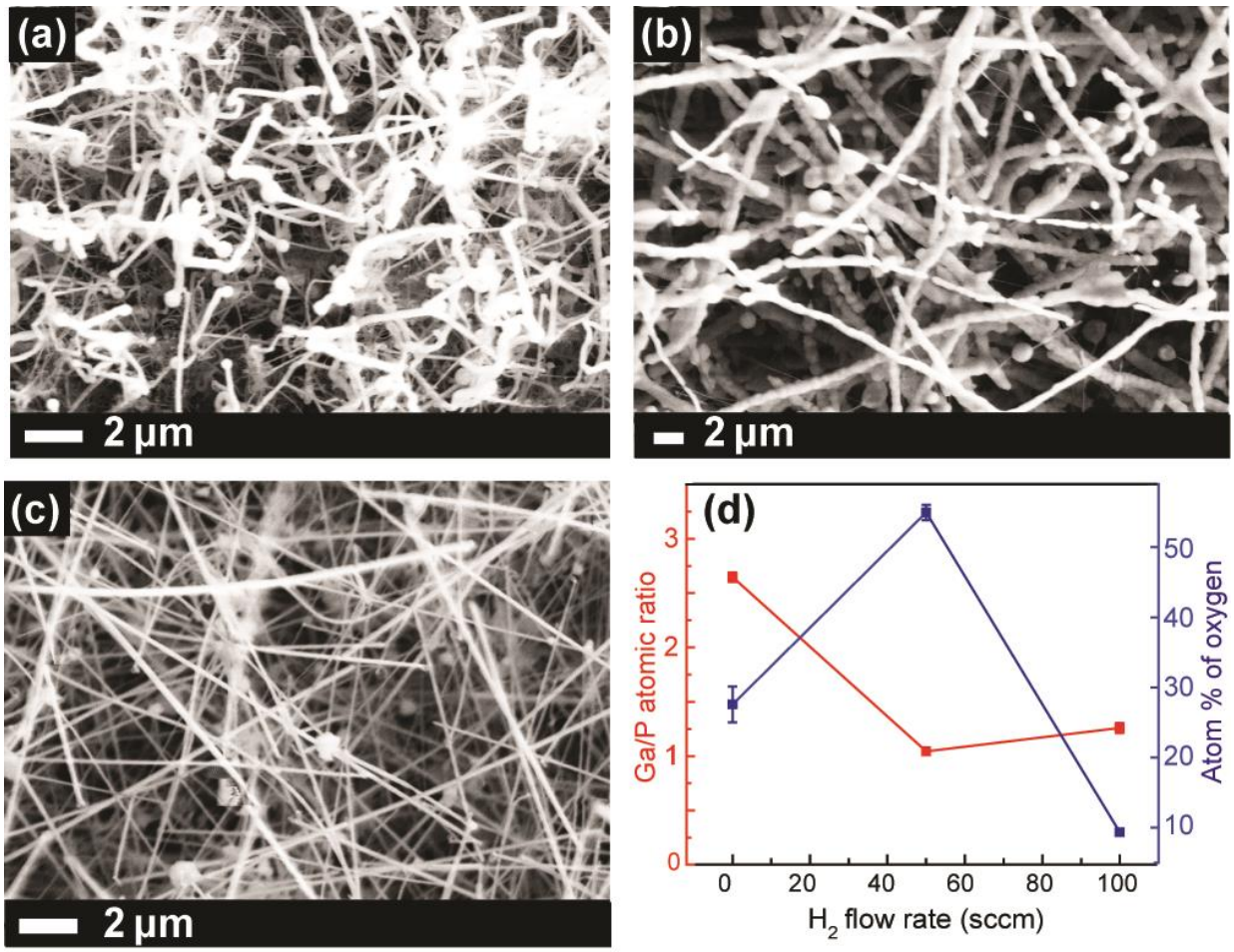

Figure 4.3 (a-c) SEM images of GaP NWs prepared at 1050 °C with flux ratio Ga:GaP=1:1 and different hydrogen flow rates: (a) 0 sccm, (b) 50 sccm, and (c) 100 sccm. (d) Dependence of Ga/P atomic ratio (red squares) and oxygen content (blue squares) in NWs on the hydrogen flow rate.

4.3 Influence of Synthesis Temperature on the NW Growth

The quantitative analysis of NWs in Figure 4.2 (a) and Figure 4.3 (a), synthesized at different temperatures but otherwise under identical conditions, indicates a lower concentration of oxygen as higher temperature. It suggests that increase in temperature could also be a positive factor in eliminating the formation of oxide shell. SEM images of GaP NWs synthesized with the precursor flux ratio Ga: GaP=1 and 100 sccm hydrogen flow at 950 °C, 1000 °C, 1050 °C are shown in Figure 4.4 (a), (b), and (c), respectively. Nanowires grown at 950 °C show significant kinking together with a high phosphorus deficiency and oxygen content of over 40 % (Figure 4.4 (d)). The kinking is diminished for the sample synthesized at 1000 °C, although NWs retain a large amount of oxygen and appear to undergo thick and uneven oxide overgrowth (Figure B2 in Appendix B). One possible reason for the thick wires could be the increasing growth of core-shell structures with Ga_2O_3 coated on the surface of the GaP NWs.[80] Importantly, the Ga:P ratio is found to approach unity. Further increase in temperature to 1050 °C yields straight and long GaP NWs with smooth surfaces, nearly ideal stoichiometry, and oxygen content below 10 % (Figure 4.4 (d)). These results clearly indicate that increasing temperature helps reduce the formation of oxide overlayers in GaP NWs. However, The temperature upper-limit of the CVD equipment in the laboratory is 1050 ^{o}C. Hence this temperature is applied to the following experiments.

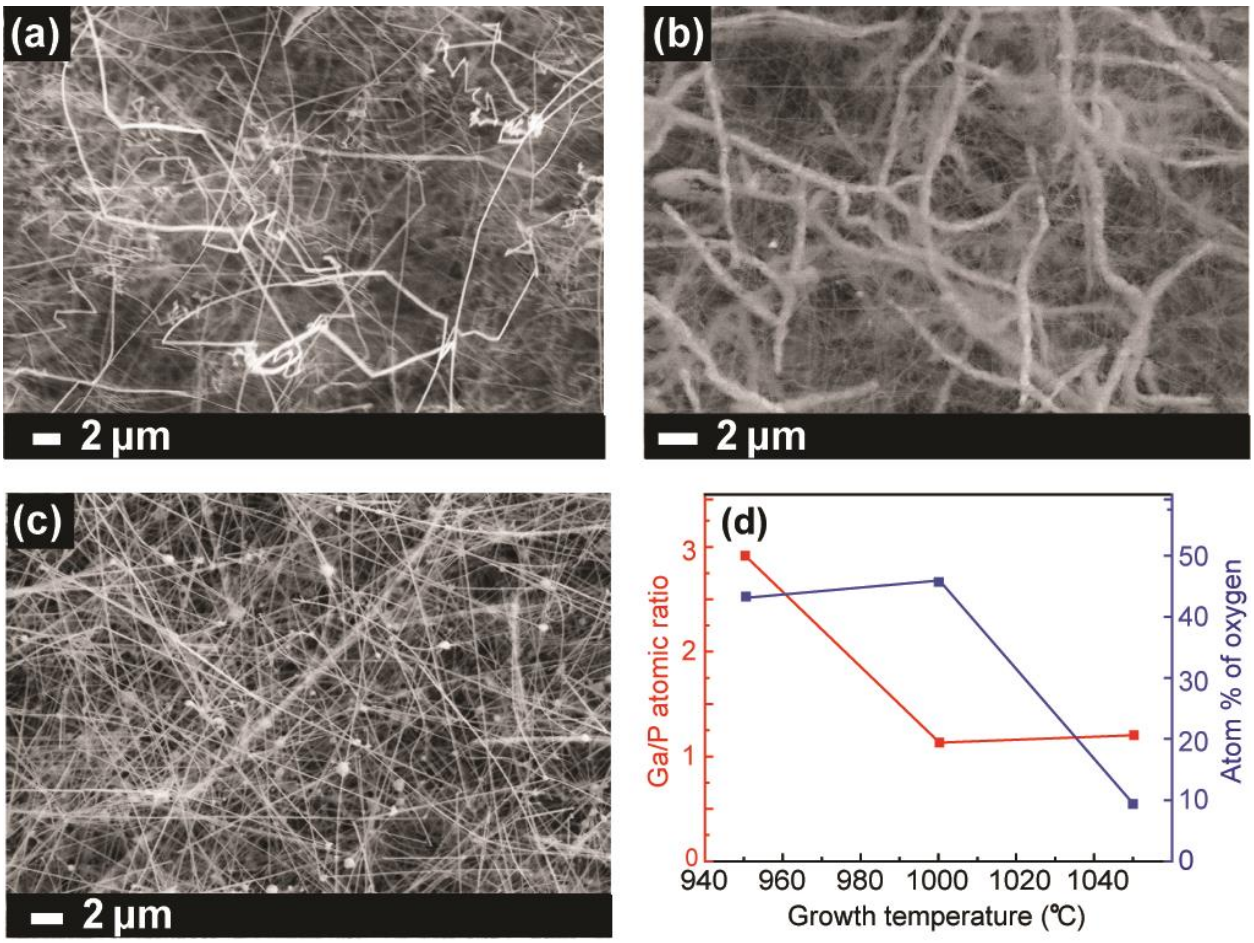

Figure 4.4 (a-c) SEM images of GaP NWs prepared with the flux ratio Ga:GaP=1:1, 100 sccm hydrogen flow rate and different temperatures: (a) 950 °C, (b) 1000 °C, and (c) 1050 °C. (d) Dependence of Ga/P atomic ratio (red squares) and oxygen content (blue squares) in NWs on the growth temperature.

4.4 Influence of Phosphorus Amount on the NW Growth

The different Ga:P ratio in the precursor mixture is also performed as a series of growth experiments. Figure 4.5 shows the results for NWs synthesized with the optimal parameters obtained above (synthesis temperature of 1050 °C, the H_2 flow rate of 100 sccm, and the total pressure of 200 Torr) but different amounts of phosphorus in the reaction mixture. While the initial amount of phosphorus does not have a notable effect on the NW growth (Figure 4.5 (a-c)) or stoichiometry (Figure 4.5 (d), red squares), an increase in the amount of phosphorus (flux ratio from P:Ga=0.5 to P:Ga=2) reduces oxygen content in NWs from about 10 % to below 1 % (Fig. 4d, blue squares). The NWs in Figure 4.5 (c) represent, to our knowledge, the first example of oxide-shell-free stoichiometric GaP NWs synthesized by a simple CVD method. It should be noted that GaP NW growth by CVD in previously reported studies was performed in either stoichiometric amounts of Ga and P or in excess of Ga. However, the extra amount of Ga may lead to an increase in oxygen layer and form unwanted shells. The results from above experiments indicate that excess of phosphorus represents a viable approach to obtaining high-quality GaP NWs that do not contain oxide overlayers.

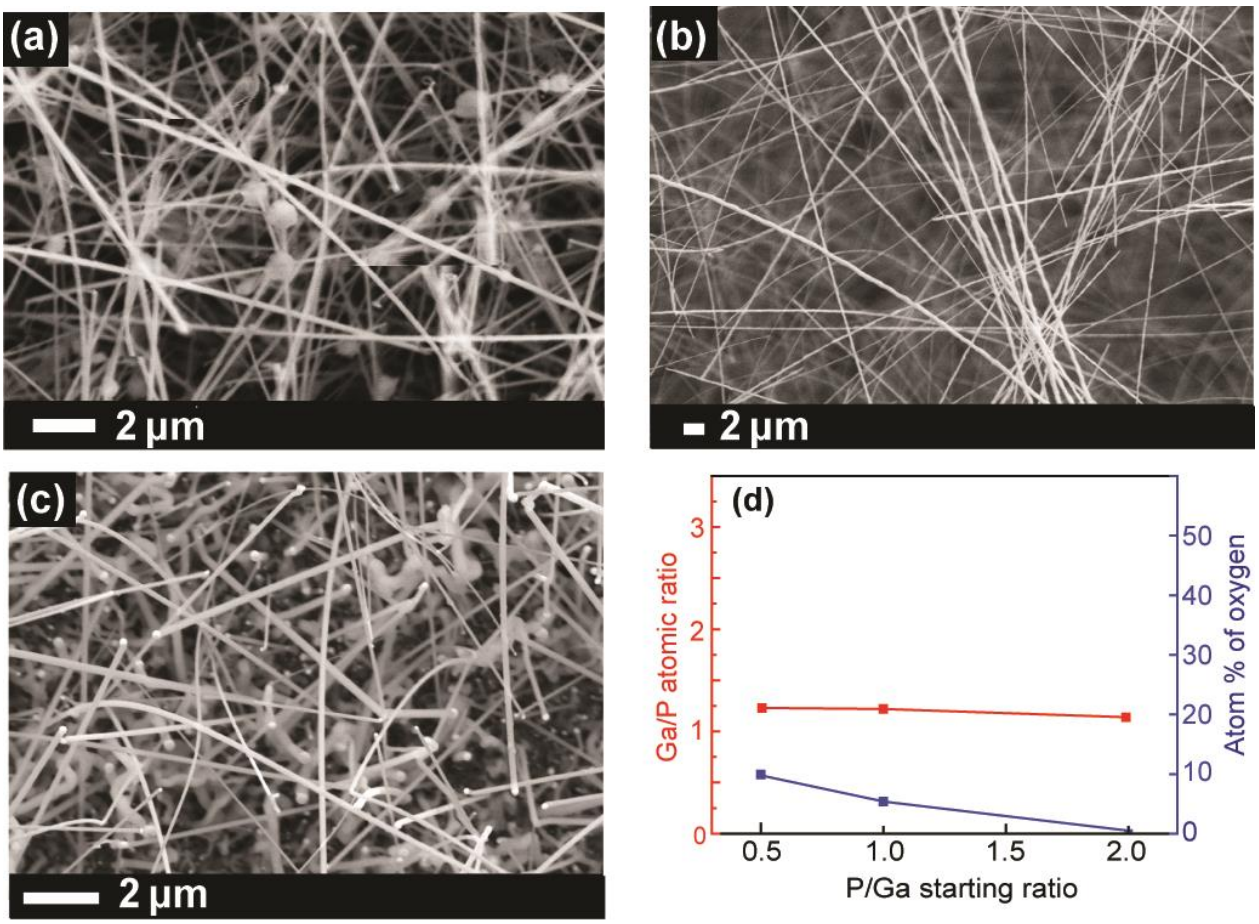

Figure 4.5 (a-c) SEM images of GaP NWs prepared at 1050 °C with 100 sccm hydrogen flow rate and P:Ga flux ratios of (a) 1:2, (b) 1:1, and (c) 2:1. (d) Dependence of Ga/P atomic ratio (red squares) and oxygen content (blue squares) in NWs on P: Ga flux ratio.

4.5 Crystal Structure and Morphology of GaP NWs under the Best Growth Condition

To confirm the structure, composition, and crystallinity of individual NWs in Figure 4.5 (c), several measurements are observed under the growth condition of 1050 ^{o}C, with 100 sccm hydrogen flow and the flux ratio P:Ga of 2. Figure 4.6 shows the XRD pattern of these NWs which confirms the zinc blende crystal structure and the absence of secondary crystal phases on the NW surfaces or growth substrate compared with Figure 4.1.

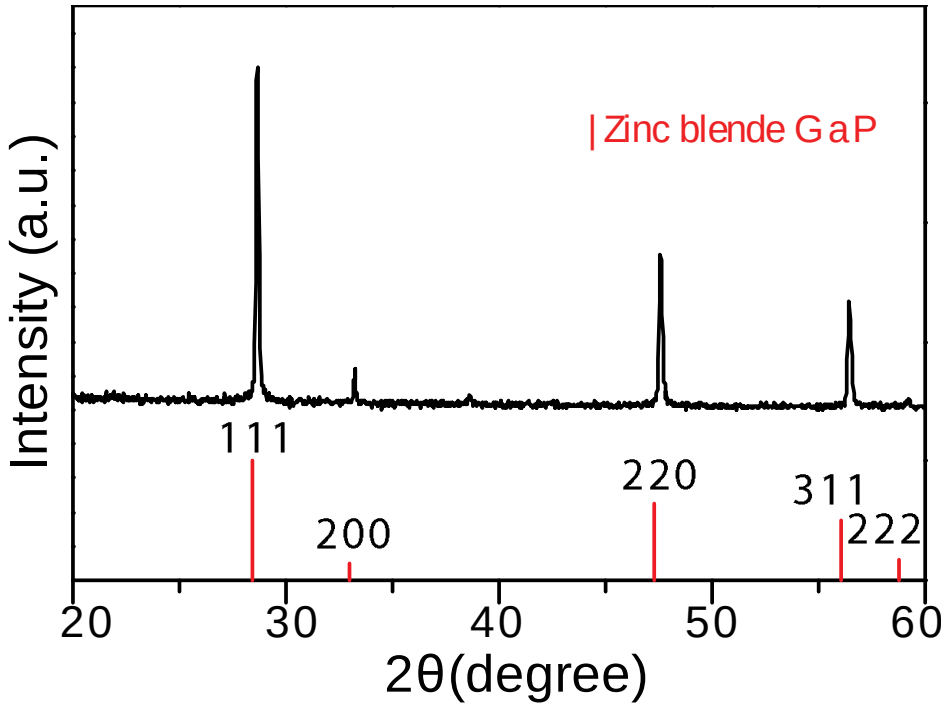

Figure 4.6 XRD pattern of GaP NWs corresponding to the SEM image in Figure 4.5 (c). Red lines correspond to the XRD pattern of bulk zinc blende GaP (JCPDS 12-0191).

Illustrated in Figure 4.7 (a), the high-resolution TEM image based on the NWs in Figure 4.5 (c) also confirms that the oxide layer is completed removed and indicates high crystallinity along the entire NW. The NW is characterized by twinning along the growth axis (Figure B3 in Appendix B), as observed previously in zinc blende GaP NWs.[75,77,82] It grows along <111> direction as shown in Figure 4.7 (c), similar to NWs in Figure 4.2 (c) prepared in the absence of hydrogen flow and excess of phosphorus.

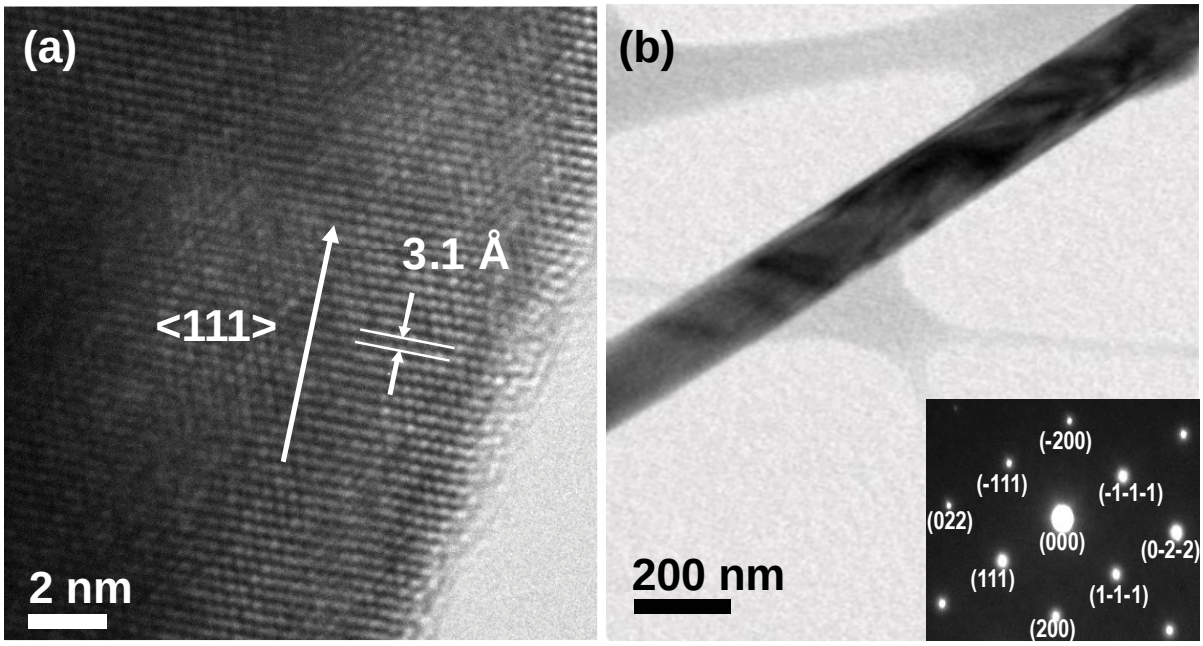

Figure 4.7 (a) High-resolution TEM image of NW from Figure 4.5 (c), showing an average lattice spacing corresponding to <111> plane. (b) TEM image and the corresponding SAED of the NW in (a) indicating <111> growth direction.

The typical EDX elemental line scan corresponds to Figure 4.7 are also observed to identify the elemental position of the NWs. As illustrated in Figure 4.8 (a) the perpendicular direction and in Figure 4.8 (b) along the NW growth direction, the Ga and P line scans have essentially the same form, as expected for the fully stoichiometric GaP NWs which is the ratio of Ga:P at 1:1. In contrast, the signal for oxygen is negligible across the NW, which in accordance with the previous SEM results.

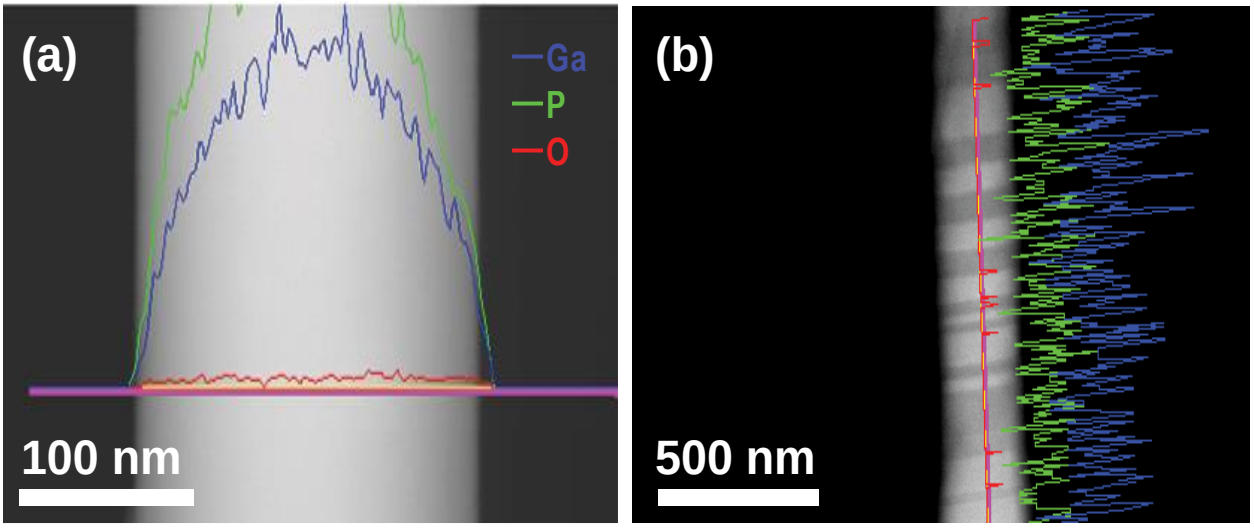

Figure 4.8 EDX elemental line scan profiles of the typical GaP NW in Figure 4.7 (a) perpendicular and (b) along the NW growth direction. The blue trace represents Ga, green trace represents P, and the red trace represents O.

4.6 Raman Spectroscopy of Bulk GaP and GaP NWs

The effect of the oxide coating on the NW structure and properties and the importance of controlling its formation was demonstrated by a series of Raman spectroscopy measurements. Figure 4.9 compares the Raman spectra of bulk GaP, oxide-coated NWs in Figure 4.1, and GaP NWs in Figure 4.5 (c) synthesized under optimized conditions. The spectrum of bulk GaP shows two characteristic peaks at 367 and 403 cm^{-1}, which can be assigned to transversal optical (TO) and longitudinal optical (LO) modes, respectively. The peaks for both TO and LO modes are broadened and shifted by 5 and 8 cm^{-1} respectively in the case of NWs, indicating that the Raman spectrum is affected by one-dimensional morphology.[100-102] Importantly, the NW spectra show an additional shoulder between TO and LO bands. This new feature is assigned to surface optical (SO) phonons, which can be activated by the NW diameter modulation.[100,101] The SO band of GaP NWs has been shown to be sensitive to the dielectric constant of the surrounding medium[100]; it broadens, increases in intensity, and redshifts with increasing dielectric constant. To assess the influence of the oxide coating on the dielectric properties of GaP NWs, the SO bands were deconvoluted by fitting the Raman spectra to a linear combination of three Lorentzian functions (Figure 4.9, thin colored lines indicated in the graph). The SO band is significantly broader and more pronounced in oxide-coated NWs (yellow traces), consistent with an increased dielectric constant of the amorphous oxide coating relative to air. The results in Figure 4.9 represent the first comparison between the Raman spectra of GaP NWs with and without oxide coating, synthesized by CVD. These results suggest the GaP NW structure and properties are strongly influenced by the oxide overlayers and emphasize the importance of controlling the formation of such coating during NW growth.

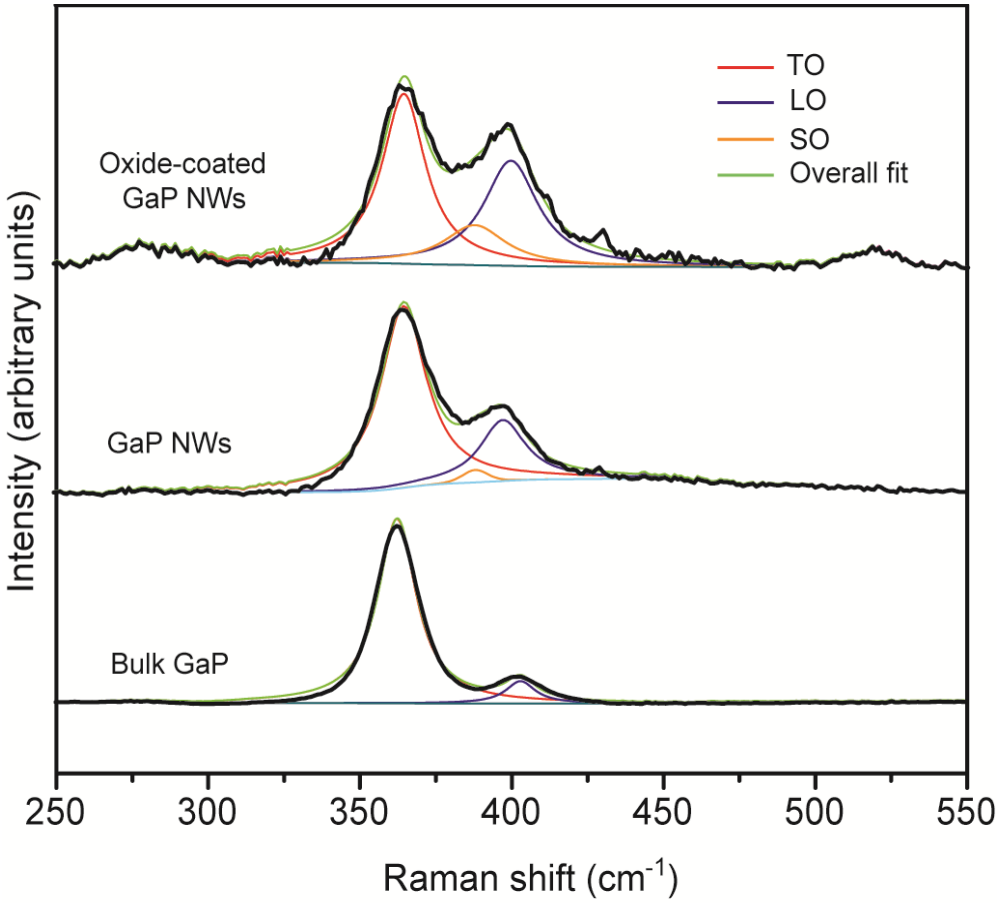

Figure 4.9 Raman spectra of bulk GaP (bottom), GaP NWs synthesized under optimized conditions for the removal of oxide overlayers (middle), and oxygen-coated NWs from Figure 4.2 (top). Raman spectra are fit to three Lorentzian functions representing TO (red line), LO (blue line), and SO (orange line) modes, respectively. Overall fit to the experimental spectra is shown with the green line.

4.7 Conclusion

In summary, in this section, a systematic study of the growth of GaP NWs by the CVD method was performed for the first time. The NW structure, morphology, and composition for the syntheses was investigated at varying growth temperature, Ga/P precursor ratio, and hydrogen flow. Increase in the growth temperature, hydrogen flow rate and the amount of phosphorous in the reaction mixture was generally conducive to the preparation of long and straight NWs with nearly ideal Ga:P stoichiometry, and without the formation of Ga_2O_3 and/or $GaPO_4$ overlayers, typically observed in the CVD growth of GaP NWs. The optimal NW structure and stoichiometry were obtained for the NWs grown at 1050 °C, with 100 sccm hydrogen flow and excess of phosphorus (P: Ga flux ratio of 2). Importantly, hydrogen flow, which has not been considered in the previously reported work involving CVD synthesis of GaP NWs, proved to be very effective in minimizing the formation of oxide overlayers. Furthermore, contrary to the previous reports which mostly rely on excess Ga in the NW synthesis, the results of this work indicate the importance of excess phosphorus for obtaining high-quality oxygen-free GaP NWs. The key factor in the elimination of the oxide overlayers is the synthesis under reducing conditions, which is in this case ensured by the introduction of hydrogen gas flow. The excess phosphorus also helps this cause by forcing the GaP formation and outcompeting the reaction of Ga with O in the growth process. The presence of the oxide overlayers significantly changes the dielectric constant of the surrounding medium as well as the electronic structure of the NWs, underlying the necessity of its rational control during NW growth. The results of this section allow for the simple and scalable synthesis of technologically important III-V NW system with optimal structure and composition, by chemically controlling the NW growth via control of the multi-parameter reaction space. The

general approach and conditions in this section are anticipated to be used for optimizing the structure and properties of other non-oxide-based semiconductor NWs, synthesized by CVD.

Future Work

Doped ZnO semiconductors are prominent nanomaterials in various studies since ZnO are earth-abundant and cost-effective. In this thesis, the plasmonic and magnetoplasmonic properties of IZO and AZO NCs have been preliminarily explored, and many conducive experiments are worthwhile to be further studied. Remaining challenges for doped plasmonic ZnO system are the relative low plasmonic intensity and poor doping efficiency. One possible research direction could be focused on overcoming these problems either via optimize current synthesis steps or attempt different synthesis methods. Besides, to enrich the positions of LSPR in the near-to-mid infrared region, new dopant precursors such as $Ga(acac)_3$ can be introduced.

Furthermore, more experiments are also needed to elucidate the mechanism of plasmon-induced carrier polarization observed in MCD experiments. Specifically, additional MCD spectra should be collected on doped ZnO NCs having different doping concentration, as well as pure ZnO NCs, prepared under different conditions such as oxidation or reducing atmosphere and having different density of native defects. These comprehensive experimental results will be supported by theoretical simulation of phonon modes and their temperature dependence, to test the hypothesis of phonon-mediated band splitting in plasmonic semiconductor NCs.

GaP NWs were successfully synthesized without oxide overlayers by CVD. Based on this result, rational improvement of the growth conditions for other types of semiconductor NWs is worthwhile to explore using the CVD method. Furthermore, since GaP NWs are promising materials in various application, it is necessary to attempt different dopants into the NWs to achieve multifunctional property in single-phase 1D semiconductor materials. One possible research route

would be to compare the experimental efficiency and realistic feasibility for the same nanomaterial on different dimensions, such as LSPR properties on ZnO NCs and NWs, which helps to further understand and improve the materials for different practical requirements.

References

(1) Melander, E.; Östman, E.; Keller, J.; Schmidt, J.; Papaioannou, E. T.; Kapaklis, V.; Arnalds, U. B.; Caballero, B.; García-Martín, A.; Cuevas, J. C. *Appl. Phys. Lett.* **2012**, *101*, 063107.

(2) Uchida, H.; Masuda, Y.; Fujikawa, R.; Baryshev, A.; Inoue, M. *J. Magn. Magn. Mater.* **2009**, *321*, 843.

(3) Stipe, B. C.; Strand, T. C.; Poon, C. C.; Balamane, H.; Boone, T. D.; Katine, J. A.; Li, J.-L.; Rawat, V.; Nemoto, H.; Hirotsune, A. *Nature photonics* **2010**, *4*, 484.

(4) Maccaferri, N.; González-Díaz, J. B.; Bonetti, S.; Berger, A.; Kataja, M.; Van Dijken, S.; Nogués, J.; Bonanni, V.; Pirzadeh, Z.; Dmitriev, A. *Opt. Express* **2013**, *21*, 9875.

(5) Fang, M.; Han, N.; Wang, F.; Yang, Z.-x.; Yip, S.; Dong, G.; Hou, J. J.; Chueh, Y.; Ho, J. C. *J Nanomater.* **2014**, *2014*.

(6) Suresh, S. *J. Nanosci. Nanotechnol.* **2013**, *3*, 62.

(7) Greiner, R. A. **1961**.

(8) West, A. R. *Basic solid state chemistry*; John Wiley & Sons Inc, 1999.

(9) Ekimov, A.; Kudryavtsev, I.; Ivanov, M.; Efros, A. L. *J. Lumin.* **1990**, *46*, 83.

(10) Dalpian, G. M.; Chelikowsky, J. R. *Phys. Rev. Lett.* **2006**, *96*, 226802.

(11) Turnbull, D. *J. Appl. Phys.* **1950**, *21*, 1022.

(12) Erwin, S. C.; Zu, L.; Haftel, M. I.; Efros, A. L. *Nature* **2005**, *436*, 91.

(13) Yogamalar, N. R.; Bose, A. C. *Appl. Phys. A* **2011**, *103*, 33.

(14) Wang, J.; An, X.; Li, Q.; Egerton, R. *Appl. Phys. Lett.* **2005**, *86*, 201911.

(15) Gu, Y.; Kuskovsky, I. L.; Yin, M.; O'Brien, S.; Neumark, G. *Appl. Phys. Lett.* **2004**, *85*, 3833.

(16) Mayer, K. M.; Hafner, J. H. *Chem. Rev.* **2011**, *111*, 3828.

(17) Kreibig, U.; Vollmer, M. In *Optical Properties of Metal Clusters*; Springer: 1995.

(18) Raether, H. In *Surface plasmons on smooth and rough surfaces and on gratings*; Springer: 1988, p 4.

(19) Zijlstra, P.; Orrit, M. *Rep. Prog. Phys.* **2011**, *74*, 106401.

(20) Giannini, V.; Fernández-Domínguez, A. I.; Heck, S. C.; Maier, S. A. *Chem. Rev.* **2011**, *111*, 3888.

(21) Hessel, C. M.; Pattani, V. P.; Rasch, M.; Panthani, M. G.; Koo, B.; Tunnell, J. W.; Korgel, B. A. *Nano Lett.* **2011**, *11*, 2560.

(22) Faucheaux, J. A.; Stanton, A. L.; Jain, P. K. *The journal of physical chemistry letters* **2014**, *5*, 976.

(23) Zhao, Y.; Pan, H.; Lou, Y.; Qiu, X.; Zhu, J.; Burda, C. *J. Am. Chem. Soc.* **2009**, *131*, 4253.

(24) Buonsanti, R.; Llordes, A.; Aloni, S.; Helms, B. A.; Milliron, D. J. *Nano Lett.* **2011**, *11*, 4706.

(25) Wan, Q.; Dattoli, E. N.; Lu, W. *Appl. Phys. Lett.* **2007**, *90*, 222107.

(26) Fang, H.; Hegde, M.; Yin, P.; Radovanovic, P. V. *Chem. Mater.* **2017**.

(27) Lounis, S. D.; Runnerstrom, E. L.; Llordés, A.; Milliron, D. J. *The journal of physical chemistry letters* **2014**, *5*, 1564.

(28) Fox, M.; Oxford University Press, Oxford: 2001.

(29) Niezgoda, J. S.; Rosenthal, S. J. *ChemPhysChem* **2016**, *17*, 645.

(30) Underwood, S.; Mulvaney, P. *Langmuir* **1994**, *10*, 3427.

(31) Kelly, K. L.; Coronado, E.; Zhao, L. L.; Schatz, G. C.; ACS Publications: 2003.

(32) Hu, M.; Novo, C.; Funston, A.; Wang, H.; Staleva, H.; Zou, S.; Mulvaney, P.; Xia, Y.; Hartland, G. V. *J. Mater. Chem.* **2008**, *18*, 1949.

(33) Armelles, G.; Cebollada, A.; García-Martín, A.; González, M. U. *Advanced Optical Materials* **2013**, *1*, 10.

(34) Uchida, K.; Adachi, H.; Kikuchi, D.; Ito, S.; Qiu, Z.; Maekawa, S.; Saitoh, E. *Nature communications* **2015**, *6*.

(35) Tse, W.-K.; MacDonald, A. *Phys. Rev. Lett.* **2010**, *105*, 057401.

(36) Chiu, K.; Quinn, J. *Physical Review B* **1972**, *5*, 4707.

(37) Chau, K.; Dice, G.; Elezzabi, A. *Phys. Rev. Lett.* **2005**, *94*, 173904.

(38) Gallo, J.; García, I.; Padro, D.; Arnáiz, B.; Penadés, S. *J. Mater. Chem.* **2010**, *20*, 10010.

(39) Liu, H.; Hou, P.; Wu, J. *J. Mater. Res.* **2011**, *26*, 2040.

(40) Pineider, F.; Campo, G.; Bonanni, V.; de Julián Fernández, C. s.; Mattei, G.; Caneschi, A.; Gatteschi, D.; Sangregorio, C. *Nano Lett.* **2013**, *13*, 4785.

(41) Ishikawa, Y.; Yao, H. *Chem. Phys. Lett.* **2014**, *609*, 93.

(42) Farvid, S. S.; Sabergharesou, T.; Hutfluss, L. N.; Hegde, M.; Prouzet, E.; Radovanovic, P. V. *J. Am. Chem. Soc.* **2014**, *136*, 7669.

(43) Schimpf, A. M.; Thakkar, N.; Gunthardt, C. E.; Masiello, D. J.; Gamelin, D. R. *ACS nano* **2013**, *8*, 1065.

(44) Özgür, Ü.; Alivov, Y. I.; Liu, C.; Teke, A.; Reshchikov, M.; Doğan, S.; Avrutin, V.; Cho, S.-J.; Morkoc, H. *J. Appl. Phys.* **2005**, *98*, 11.

(45) Yang, Z.; Chu, S.; Chen, W. V.; Li, L.; Kong, J.; Ren, J.; Paul, K.; Liu, J. *Applied physics express* **2010**, *3*, 032101.

(46) Look, D. C. *Materials Science and Engineering: B* **2001**, *80*, 383.

(47) Yibi, Y.; Chen, J.; Xue, J.; Song, J.; Zeng, H. *Science Bulletin* **2017**.

(48) Chouchene, B.; Chaabane, T. B.; Mozet, K.; Girot, E.; Corbel, S.; Balan, L.; Medjahdi, G.; Schneider, R. *Appl. Surf. Sci.* **2017**, *409*, 102.

(49) Greenberg, B. L.; Ganguly, S.; Held, J. T.; Kramer, N. J.; Mkhoyan, K. A.; Aydil, E. S.; Kortshagen, U. R. *Nano Lett.* **2015**, *15*, 8162.

(50) Della Gaspera, E.; Chesman, A. S.; van Embden, J.; Jasieniak, J. J. *ACS nano* **2014**, *8*, 9154.

(51) Li, A.; Zou, J.; Han, X. *Science China Materials* **2016**, *59*, 51.

(52) Wallentin, J.; Borgström, M. T. *J. Mater. Res.* **2011**, *26*, 2142.

(53) Dai, X.; Messanvi, A.; Zhang, H.; Durand, C.; Eymery, J.; Bougerol, C.; Julien, F. H.; Tchernycheva, M. *Nano Lett.* **2015**, *15*, 6958.

(54) Saxena, D.; Mokkapati, S.; Parkinson, P.; Jiang, N.; Gao, Q.; Tan, H. H.; Jagadish, C. *Nature Photonics* **2013**, *7*, 963.

(55) Hegde, M.; Farvid, S. S.; Hosein, I. D.; Radovanovic, P. V. *Acs Nano* **2011**, *5*, 6365.

(56) Stamplecoskie, K. G.; Ju, L.; Farvid, S. S.; Radovanovic, P. V. *Nano Lett.* **2008**, *8*, 2674.

(57) Ishizaka, F.; Hiraya, Y.; Tomioka, K.; Fukui, T. *J. Cryst. Growth* **2015**, *411*, 71.

(58) Braun, W.; Kaganer, V. M.; Trampert, A.; Schönherr, H.-P.; Gong, Q.; Nötzel, R.; Däweritz, L.; Ploog, K. H. *J. Cryst. Growth* **2001**, *227*, 51.

(59) Verheijen, M. A.; Algra, R. E.; Borgström, M. T.; Immink, G.; Sourty, E.; van Enckevort, W. J.; Vlieg, E.; Bakkers, E. P. *Nano Lett.* **2007**, *7*, 3051.

(60) Berger, L. I. *Semiconductor materials*; CRC press, 1996.

(61) Assali, S.; Zardo, I.; Plissard, S.; Kriegner, D.; Verheijen, M.; Bauer, G.; Meijerink, A.; Belabbes, A.; Bechstedt, F.; Haverkort, J. *Nano Lett.* **2013**, *13*, 1559.

(62) Hara, T.; Akasaki, I. *J. Appl. Phys.* **1968**, *39*, 285.

(63) Liu, C.; Sun, J.; Tang, J.; Yang, P. *Nano Lett.* **2012**, *12*, 5407.

(64) Yamaguchi, M.; Takamoto, T.; Araki, K.; Ekins-Daukes, N. *Solar Energy* **2005**, *79*, 78.

(65) Hochbaum, A. I.; Yang, P. *Chem. Rev.* **2009**, *110*, 527.

(66) Dick, K. A.; Deppert, K.; Larsson, M. W.; Mårtensson, T.; Seifert, W.; Wallenberg, L. R.; Samuelson, L. *Nature materials* **2004**, *3*, 380.

(67) Xia, Y.; Yang, P.; Sun, Y.; Wu, Y.; Mayers, B.; Gates, B.; Yin, Y.; Kim, F.; Yan, H. *Adv. Mater.* **2003**, *15*, 353.

(68) Wagner, R.; Ellis, W. *Appl. Phys. Lett.* **1964**, *4*, 89.

(69) Law, M.; Goldberger, J.; Yang, P. *Annu. Rev. Mater. Res.* **2004**, *34*, 83.

(70) Duan, X.; Lieber, C. M. *Adv. Mater.* **2000**, *12*, 298.

(71) Givargizov, E. *J. Cryst. Growth* **1975**, *31*, 20.

(72) Shao, R.; Bonnell, D. A. *Appl. Phys. Lett.* **2004**, *85*, 4968.

(73) Fröberg, L.; Seifert, W.; Johansson, J. *Physical Review B* **2007**, *76*, 153401.

(74) Borgström, M. T.; Wallentin, J.; Trägårdh, J.; Ramvall, P.; Ek, M.; Wallenberg, L. R.; Samuelson, L.; Deppert, K. *Nano Research* **2010**, *3*, 264.

(75) Kuyanov, P.; Boulanger, J.; LaPierre, R. *J. Cryst. Growth* **2017**, *462*, 29.

(76) Cerqueira, C. F.; Viana, B. C.; da Luz-Lima, C.; Perea-Lopez, N.; Terrones, M.; Falcão, E. H.; Gomes, A. S.; Chassagnon, R.; Pinto, A. L.; Sampaio, L. C. *J. Cryst. Growth* **2015**, *431*, 72.

(77) Gu, Z.; Paranthaman, M. P.; Pan, Z. *Cryst. Growth Des.* **2008**, *9*, 525.

(78) Hosein, I. D.; Hegde, M.; Jones, P. D.; Chirmanov, V.; Radovanovic, P. V. *J. Cryst. Growth* **2014**, *396*, 24.

(79) Radovanovic, P. V.; Stamplecoskie, K. G.; Pautler, B. G. *J. Am. Chem. Soc.* **2007**, *129*, 10980.

(80) Zeng, Z.; Li, Y.; Chen, J.; Zhou, W. *The Journal of Physical Chemistry C* **2008**, *112*, 18588.

(81) Lyu, S.; Zhang, Y.; Ruh, H.; Lee, H.; Lee, C. *Chem. Phys. Lett.* **2003**, *367*, 717.

(82) Liu, B.; Bando, Y.; Tang, C.; Xu, F. *Applied Physics A: Materials Science & Processing* **2005**, *80*, 1585.

(83) Holm, J. V.; Jørgensen, H. I.; Krogstrup, P.; Nygård, J.; Liu, H.; Aagesen, M. *Nature communications* **2013**, *4*, 1498.

(84) Wang, J.; Gudiksen, M. S.; Duan, X.; Cui, Y.; Lieber, C. M. *Science* **2001**, *293*, 1455.

(85) Dhara, S.; Lu, C.-Y.; Chen, K.-H. *Plasmonics* **2015**, *10*, 347.

(86) Holzwarth, U.; Gibson, N. *Nature Nanotechnology* **2011**, *6*, 534.

(87) Ferraro, J.; Nakamoto, K.; Brown, C. W.; Academic press.

(88) Fang, T.-H.; Kang, S.-H. *Current Applied Physics* **2010**, *10*, 1076.

(89) Wang, G. Z.; Han, X. H. *J. Phys. D: Appl. Phys.* **2009**, *42*, 175308.

(90) Ghosh, S.; Saha, M.; De, S. K. *Nanoscale* **2014**, *6*, 7039.

(91) Chen, Y.; Kim, M.; Lian, G.; Johnson, M. B.; Peng, X. *J. Am. Chem. Soc.* **2005**, *127*, 13331.

(92) Yang, M.; Sun, K.; Kotov, N. A. *J. Am. Chem. Soc.* **2010**, *132*, 1860.

(93) Yusufkadie, Y.; Jiawei, C.; Jie, X.; Jizhong, S.; Haibo, Z. *Science Bulletin* **2017**, *62*, 693.

(94) Yin, P.; Tan, Y.; Fang, H.; Radovanovic, P. V. *Unpublished*.

(95) Yu, C.-F.; Sun, S.-J.; Hsu, H.-S. *Phys. Lett. A* **2015**, *379*, 211.

(96) Radović, M.; Dohčević-Mitrović, Z.; Paunović, N.; Bošković, S.; Tomić, N.; Tadić, N.; Belča, I. *J. Phys. D: Appl. Phys.* **2015**, *48*, 065301.

(97) Fedorov, A.; Baranov, A.; Inoue, K. *Physical Review B* **1997**, *56*, 7491.

(98) Beye, M.; Hennies, F.; Deppe, M.; Suljoti, E.; Nagasono, M.; Wurth, W.; Föhlisch, A. *Phys. Rev. Lett.* **2009**, *103*, 237401.

(99) O'Donnell, K.; Chen, X. *Appl. Phys. Lett.* **1991**, *58*, 2924.

(100) Gupta, R.; Xiong, Q.; Mahan, G.; Eklund, P. *Nano Lett.* **2003**, *3*, 1745.

(101) Dobrovolsky, A.; Sukrittanon, S.; Kuang, Y.; Tu, C.; Chen, W.; Buyanova, I. *Appl. Phys. Lett.* **2014**, *105*, 193102.

(102) de la Chapelle, M. L.; Han, H.; Tang, C. *The European Physical Journal B-Condensed Matter and Complex Systems* **2005**, *46*, 507.

Appendix A Doped ZnO NCs

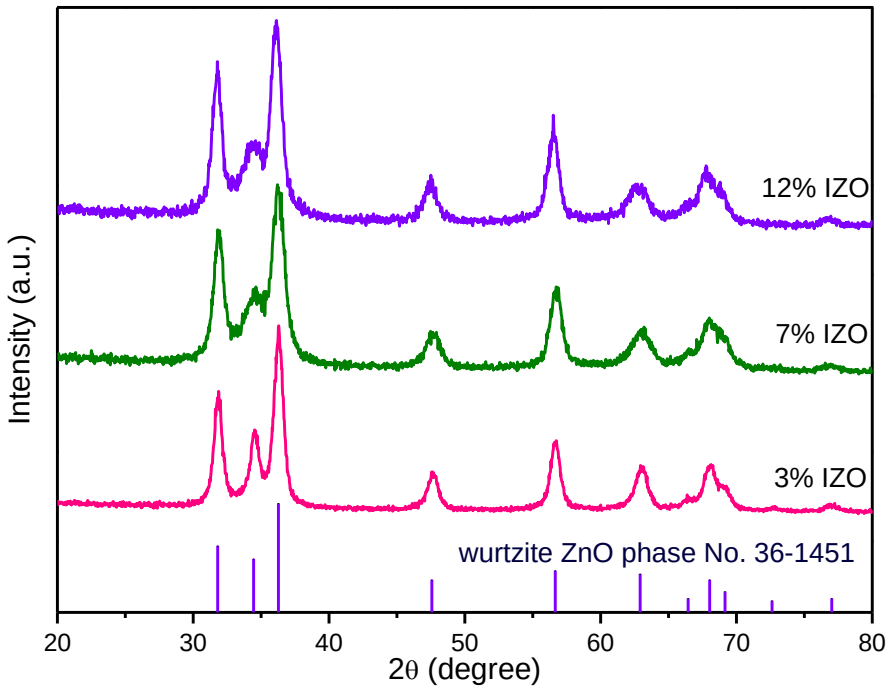

Figure A1 XRD pattern for IZO with different starting In/Zn molar ratio (3 %, 7 %, and 12 %). Purple lines correspond to the XRD pattern of bulk wurtzite ZnO (JCPDS 36-1451).

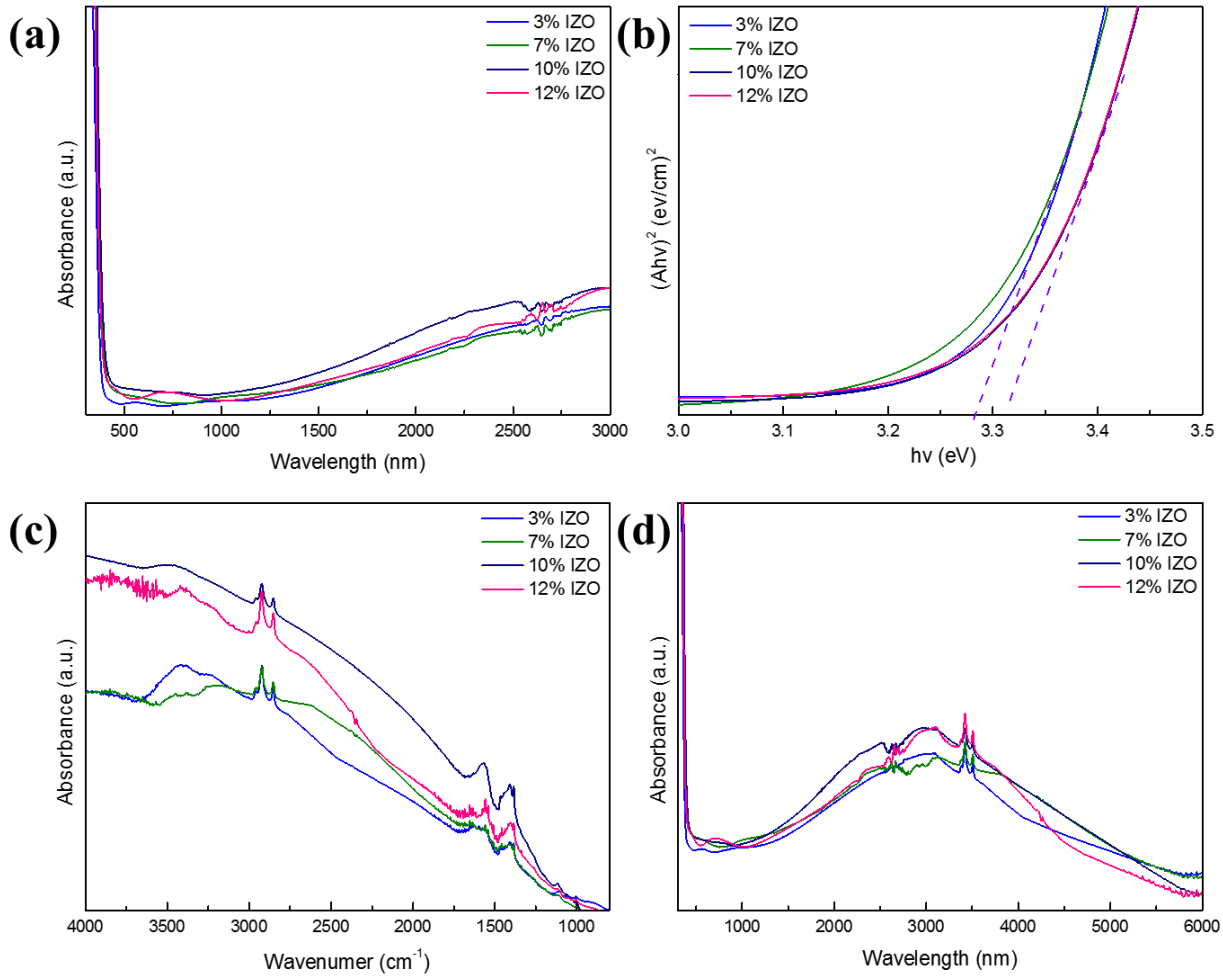

Figure A2 (a) UV-Vis-NIR absorption spectra IZO NCs normalized at band gap absorption. The In/Zn ratio are 3 %, 7 %, 10 %, and 12 %. (b)Tauc plot of the optical band gap of IZO NCs with various doping concentration (3 %, 7 %, 10 %, and 12 %) based on the UV-Vis-NIR spectra. (c) Normalized FTIR absorption spectra of IZO NCs with different staring doping concentrations of In/Zn (3 %, 7 %, 10 %, and 12 %). (d) Normalized absorption spectra of IZO NCs with different starting doping concentrations of In/Zn (3 %, 7 %, 10 %, and 12 %). The spectral range is from UV to the MIR by combining the UV-Vis-NIR spectra and the FTIR spectra together.

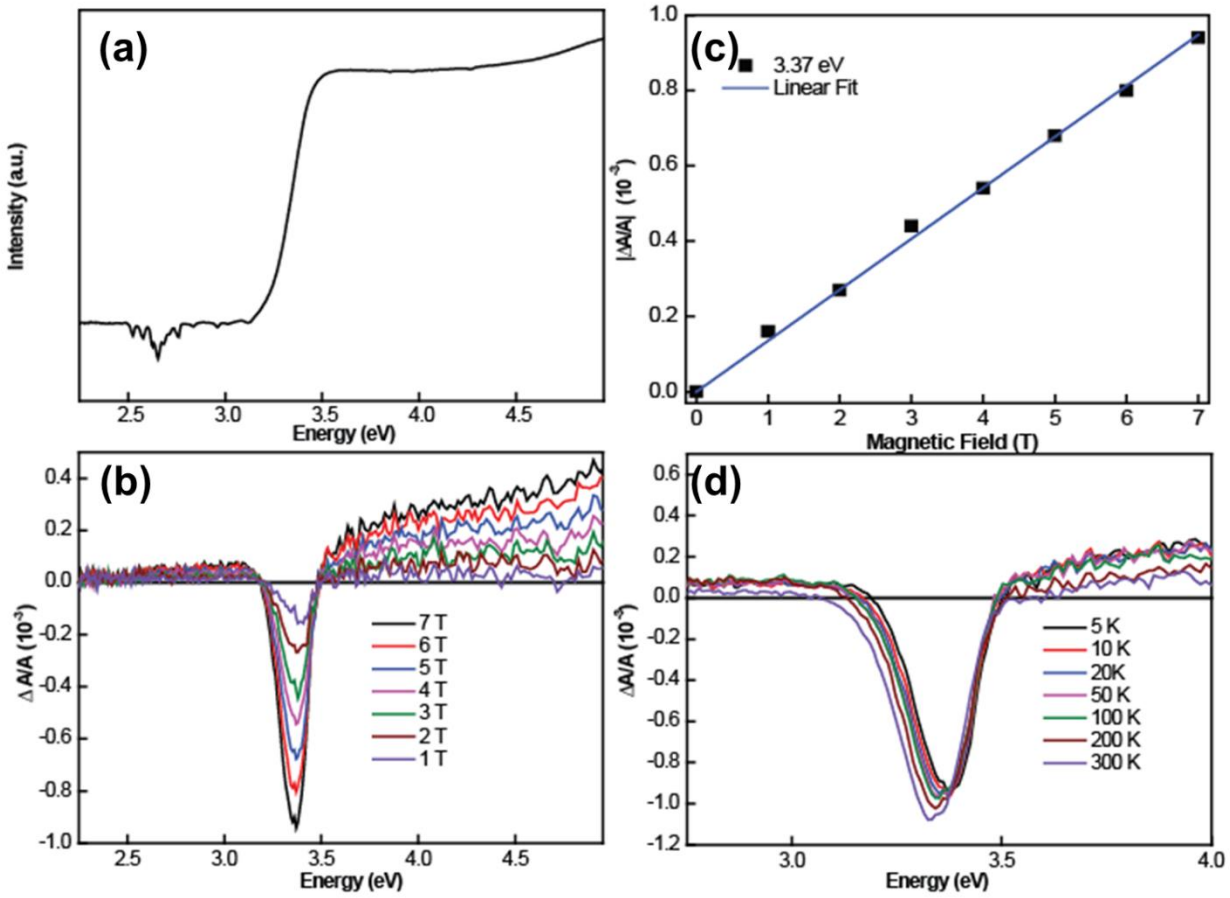

Figure A3 (a) Absorption spectra and (b) MCD spectra of 1 % IZO NCs collect at 5 K. MCD spectra collected at different external magnetic field strengths are indicated in the graph. (c) Magnetic field dependence of MCD intensity at 3.37 eV for ZnO NCs in (b) as a function of external magnetic fields. Blue solid trace is the linear fitting of the data points. (d) MCD spectra of pure ZnO NCs in (a) collected at 7 T for various temperatures (5 K – 300 K).

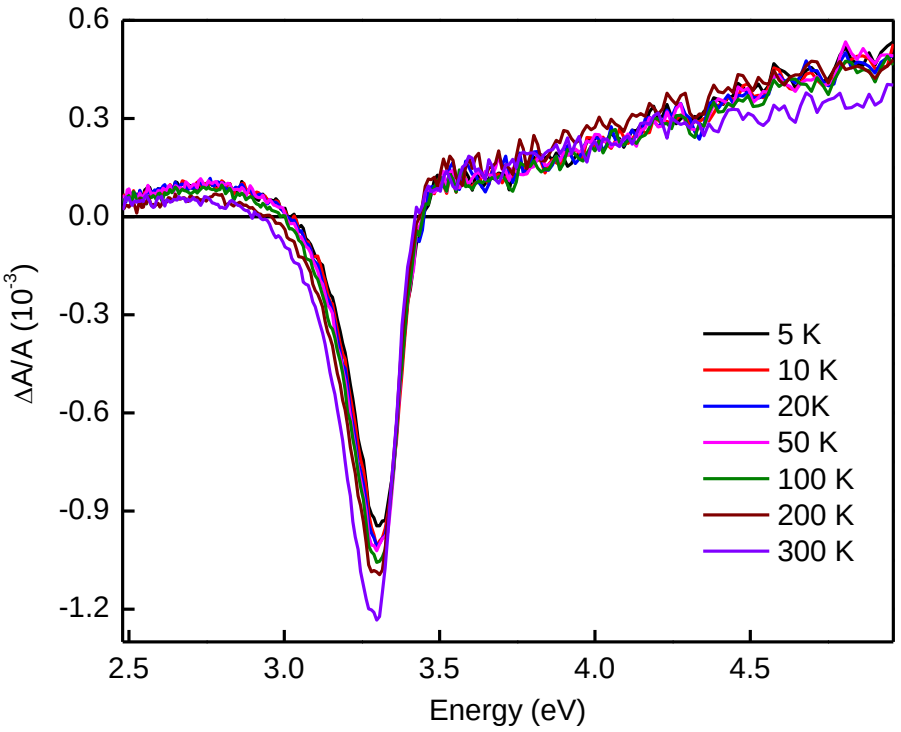

Figure A4 MCD spectra of 5 % IZO NCs in (a) collected at 7 T for various temperatures (5 K – 300 K). MCD spectra collected at different temperature are indicated in the graph.

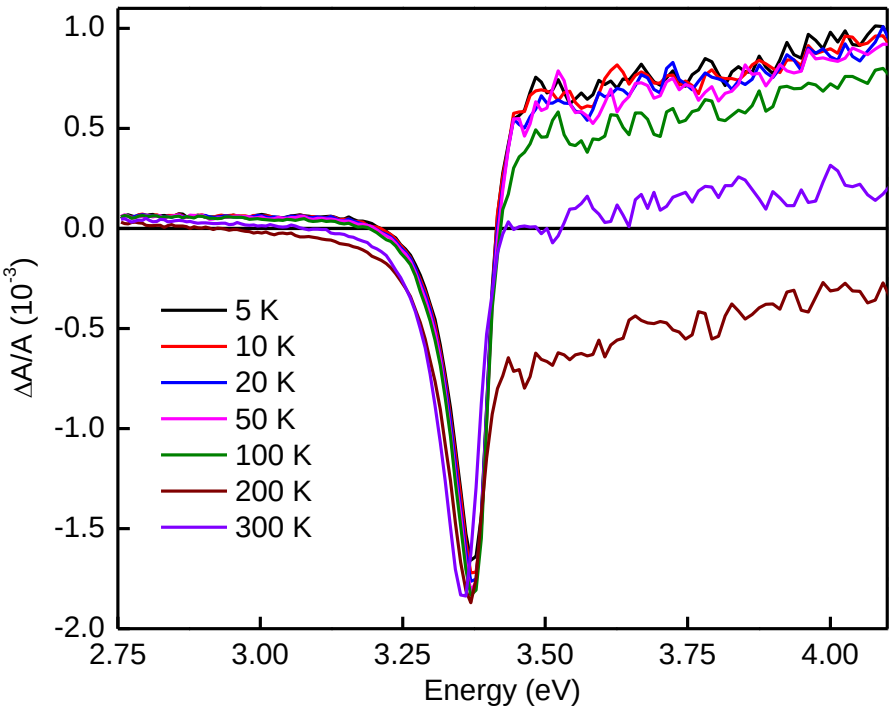

Figure A5 MCD spectra of 10% AZO NCs in (a) collected at 7 T for various temperatures (5 K – 300 K). MCD spectra collected at different temperature are indicated in the graph.

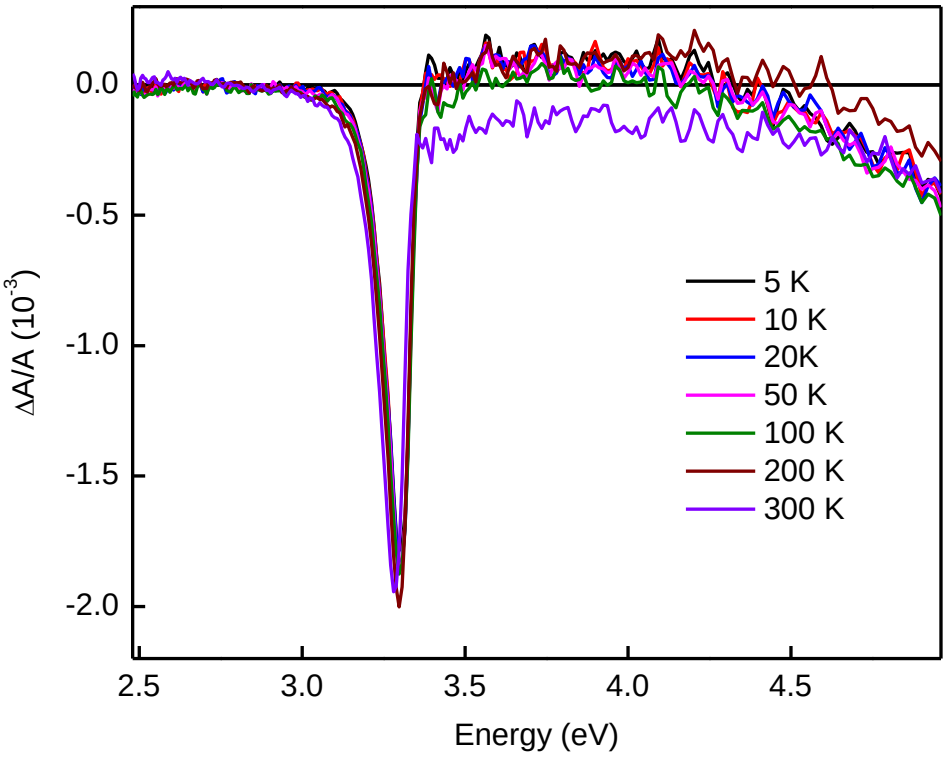

Figure A6 MCD spectra of 30 % AZO NCs in (a) collected at 7 T for various temperatures (5 K-300 K). MCD spectra collected at different temperature are indicated in the graph.

Appendix B GaP NWs Grown by CVD

Figure B1 Typical SEM imag

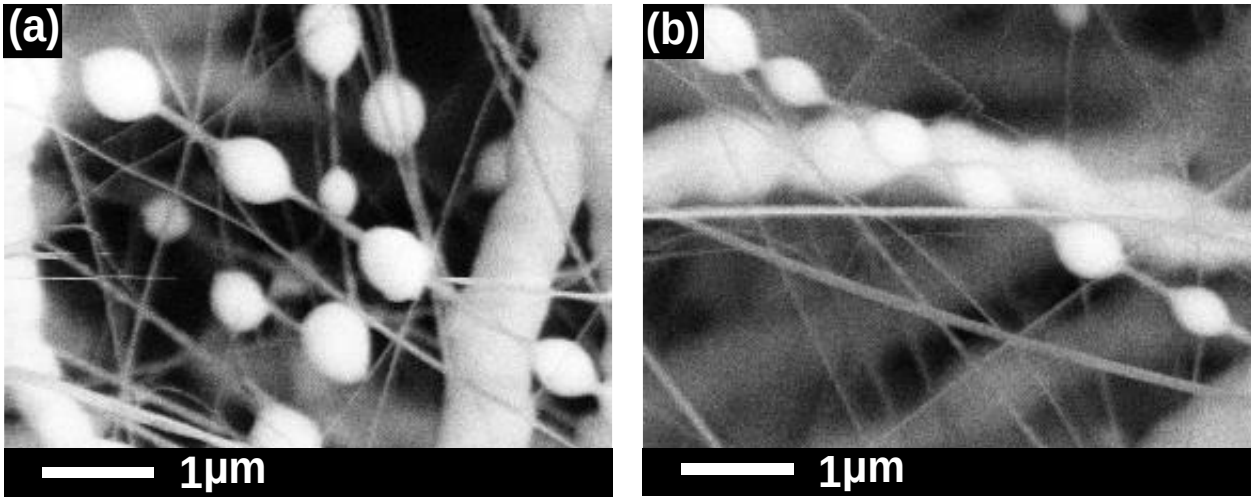

es of GaP NWs synthesized at 1050 °C, flux ratio Ga:GaP=1:1, and low-to-moderate hydrogen flow (up to 50 sccm). The images in (a) and (b) show neckless-like NW structures having a different separation between periodically spaced bumps, and different thickness of the NW core connecting the bumps.

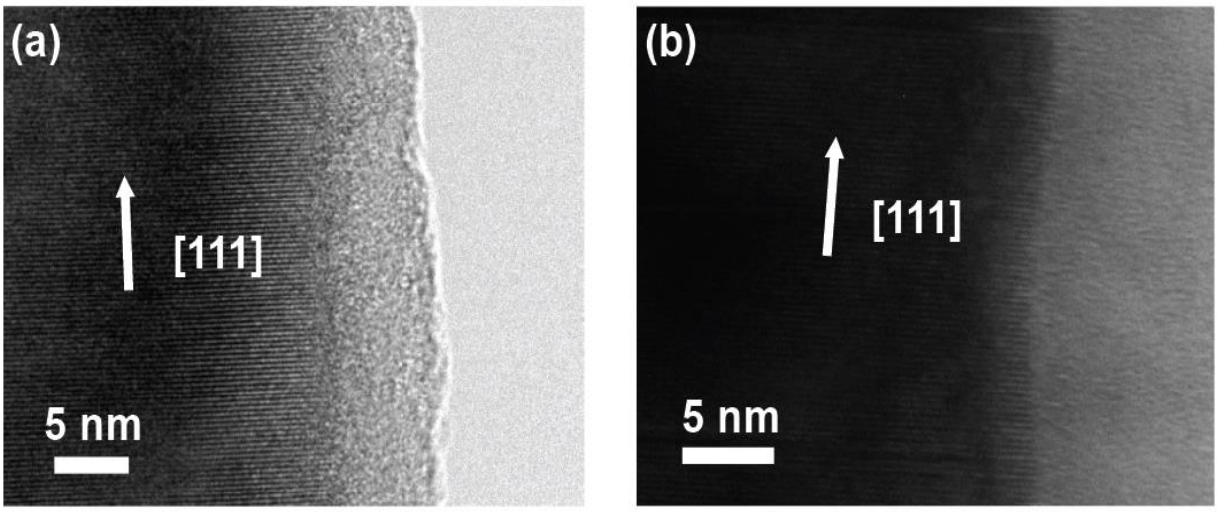

Figure B2 Representative TEM images of GaP NW synthesized at 1000 °C with the precursor flux ratio Ga:GaP=1:1 and 100 sccm hydrogen flow. The NW grows along <111> direction and contains a relatively thick amorphous oxide coating.

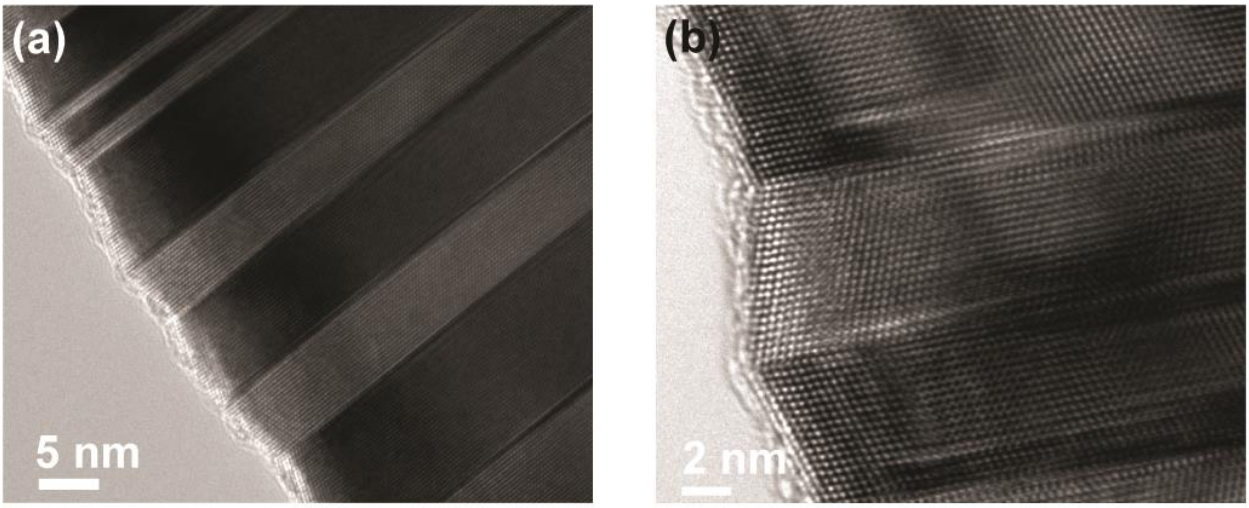

Figure B3 TEM images of GaP NWs synthesized under optimal conditions for the elimination of the oxide overlayers (1050 °C, 100 sccm hydrogen flow, and flux ratio P:Ga=2). (a) Zoom-out single NW image, and (b) lattice-resolved image.